

Role of a Cross-Barrier Jet and Turbulence on Winter Orographic Snowfall

JOSHUA AIKINS AND KATJA FRIEDRICH

*Department of Atmospheric and Oceanic Sciences, University of Colorado Boulder,
Boulder, Colorado*

BART GEERTS AND BINOD POKHAREL

Department of Atmospheric Science, University of Wyoming, Laramie, Wyoming

(Manuscript received 14 January 2016, in final form 10 May 2016)

ABSTRACT

Natural small-scale microphysical and dynamical mechanisms are identified in a winter orographic snowstorm over the Sierra Madre Range of Wyoming during an intensive observational period (IOP) from the AgI Seeding Cloud Impact Investigation (ASCI; January–March 2012). A suite of high-resolution radars, including a ground-based scanning X-band dual-polarization Doppler on Wheels radar, vertically pointing Ka-band Micro Rain Radar (MRR), and airborne W-band Wyoming Cloud Radar (WCR), and additional in situ and remote sensing instruments are used in the analysis. The analysis focuses on a deep postfrontal period on 16 January 2012 (IOP2) when clouds extended throughout the troposphere and cloud liquid water was absent following the passage of a baroclinic front. A turbulent shear layer was observed in this postfrontal environment that was created by a midlevel cross-barrier jet riding over a decoupled Arctic air mass that extended above mountaintop. MRR and WCR observations indicate additional regions of turbulence aloft that favor rapid particle growth at upper levels of the cloud. Plunging flow in the lee of the Sierra Madre was also observed during this case, which caused sublimation of snow up to 20 km downwind. The multi-instrument analysis in this paper suggests that 1) shear-induced turbulent overturning cells do exist over cold continental mountain ranges like the Sierra Madre, 2) the presence of cross-barrier jets favors these turbulent shear zones, 3) this turbulence is a key mechanism in enhancing snow growth, and 4) snow growth enhanced by turbulence primarily occurs through deposition and aggregation in these cold ($< -15^{\circ}\text{C}$) postfrontal continental environments.

1. Introduction

In many mountainous regions on Earth, snowfall accounts for a substantial portion of the total annual precipitation and its local spatial distribution becomes increasingly important for hydrometeorological applications such as evaluating flood risk, water availability, and hydropower production. Recent studies have shown that mesoscale and microscale dynamic and microphysical processes, which convert condensed water quickly and efficiently into precipitation, are becoming more important in understanding regional precipitation generation and distribution (e.g., [Rotunno and Houze 2007](#); [Garvert et al. 2007](#); [Kirshbaum et al.](#)

[2007](#); [Kumjian et al. 2014](#); [Medina and Houze 2015](#), hereafter [MH15](#)).

Microscale shear dynamic instability found in frontal systems associated with baroclinic waves has been highlighted as one such dynamic process ([Houze and Medina 2005](#), hereafter [HM05](#); [MH15](#)). These studies found that shear instability can produce so-called overturning cells, which are 1–5 km wide with updrafts of $1\text{--}3\text{ m s}^{-1}$, when wind shear exceeds $10\text{ m s}^{-1}\text{ km}^{-1}$. These updrafts can produce pockets of increased liquid water content (LWC), enhancing riming and coalescence and increasing aggregation through differences in fall velocity of forming and growing particles. These particles then grow rapidly and fall out quickly on windward slopes. [HM05](#) identified overturning cells in terrain-sloping layers of shear turbulence in stable environments with blocked or partially retarded cross-barrier orographic flow below mountaintop in the Oregon Cascades and Alps. [Medina et al. \(2005\)](#) used model

Corresponding author address: Joshua Aikins, Dept. of Atmospheric and Oceanic Sciences, University of Colorado Boulder, UCB 311, Boulder, CO 80309.
E-mail: joshua.aikins@colorado.edu

sensitivity studies to show that increased upwind stability, surface friction, mountain height, and preexisting wind shear enhance this turbulent shear zone. MH15 further studied shear-induced turbulence in cyclones crossing the California Sierra Nevada. Shear-induced turbulence was found in storms with strong upstream winds and higher vertically integrated cross- and along-barrier moisture fluxes. Similar cloud-top generating cells have also been identified (Rosenow et al. 2014; Kumjian et al. 2014; Plummer et al. 2014), but these overturning cells are more tied to convective instability rather than shear instability. Additionally, Geerts et al. (2011) observed snow growth within boundary layer turbulence on windward mountain slopes, but the aggregational growth mechanism suggested is only speculative. The lack of abundant observational and modeling research of the impacts of turbulence on microphysical processes is further motivation for this study.

Previous studies on shear instability have focused on large mountain ranges adjacent to large bodies of water with large moisture fluxes and mixed-phase precipitation. Cloud microphysical processes present in orographic environments over inland mountain ranges were found to differ from coastal mountains, mainly due to the lower and warmer cloud bases of coastal storm systems that favor riming and increased ice crystal concentrations through the rime splintering mechanism (Raubert 1992). Less riming is observed for inland mountain ranges, partly due to the fact that water is removed from the atmosphere by upwind mountain ranges (Hindman 1986; Saleeby et al. 2011), but cloud liquid water has still been observed within regions where the condensate supply rate can exceed the diffusional growth rate of ice crystals (Raubert and Grant 1986). These regions were found to be near cloud top, between cloud base and -10°C , and directly upwind and over the mountain crest where strong orographic lift is typically observed. Depositional and aggregational growth are the primary microphysical mechanisms within colder continental environments.

Do shear turbulence regions and overturning cells exist over continental mountain ranges with colder temperatures and reduced moisture fluxes? If so, do these overturning cells enhance precipitation? If enhancement occurs, through what microphysical mechanism(s) does it occur? This study aims to answer these questions by investigating the role of shear instability over the Sierra Madre Range in southern Wyoming, a small inner-mountain range with lower advected moisture fluxes.

The data used in this paper were collected during the AgI Seeding Cloud Impact Investigation (ASCII; Geerts et al. 2013). ASCII took place during January–March

2012 and was designed to observe changes in cloud microphysical properties due to ground-based seeding of orographic clouds over the Sierra Madre Range of Wyoming (Fig. 1a). Although cloud seeding effects from ASCII continue to be analyzed (e.g., Geerts et al. 2013; Pokharel et al. 2014a,b; Jing et al. 2015; Jing and Geerts 2015; Pokharel et al. 2015), the suite of surface and airborne instrumentation deployed during ASCII also provides observations of natural orographic precipitation over this Continental Divide mountain range. The analysis in this paper will largely focus on a 140-min postfrontal time period when a deep layer of clouds and precipitation associated with a passing baroclinic storm was present.

Section 2 describes the instrumentation used in the analysis as well as any data quality techniques used. Section 3 provides a brief overview for the case analyzed in this paper. Section 4 provides an overview of the precipitation observed by surface observations and the Doppler on Wheels (DOW) radar. Section 5 identifies and analyzes the impacts of a cross-barrier jet and plunging flow. Section 6 identifies regions of turbulence and analyzes its impact on precipitation processes. Section 7 provides a discussion on our findings and how they relate to previous research, and section 8 summarizes the main findings of this paper.

2. Data and methods

a. Radar

1) DOPPLER ON WHEELS DUAL-POLARIZATION X-BAND RADAR

A ground-based scanning Doppler on Wheels dual-polarization X-band radar was positioned on the Sierra Madre pass (Battle Pass, 3029 m MSL; Fig. 1a). The DOW operated at a frequency of 9.5 GHz with a beamwidth of 0.93° (Wurman 2001). The pulse duration was chosen to be $0.4 \mu\text{s}$, relating to a resolution of 60 m in range. With 800 range gates, the maximum range was 48 km. Data were sampled at 0.5° resolution in azimuth at a rate of 30°s^{-1} . The radar was run with a pulse repetition frequency (PRF) of 2500 Hz, resulting in a Nyquist velocity of 19.7 m s^{-1} . Besides reflectivity Z and Doppler velocity fields, the DOW radar provided differential reflectivity Z_{DR} , correlation coefficient ρ_{HV} , spectral width, and total differential phase Φ_{DP} . The radar scan strategy included full volume scans, or plan position indicator (PPI) scans, with elevation angles every 1° between -1° and 20° elevation, every 2° between 20° and 30° , and every 4° between 30° and 70° . In

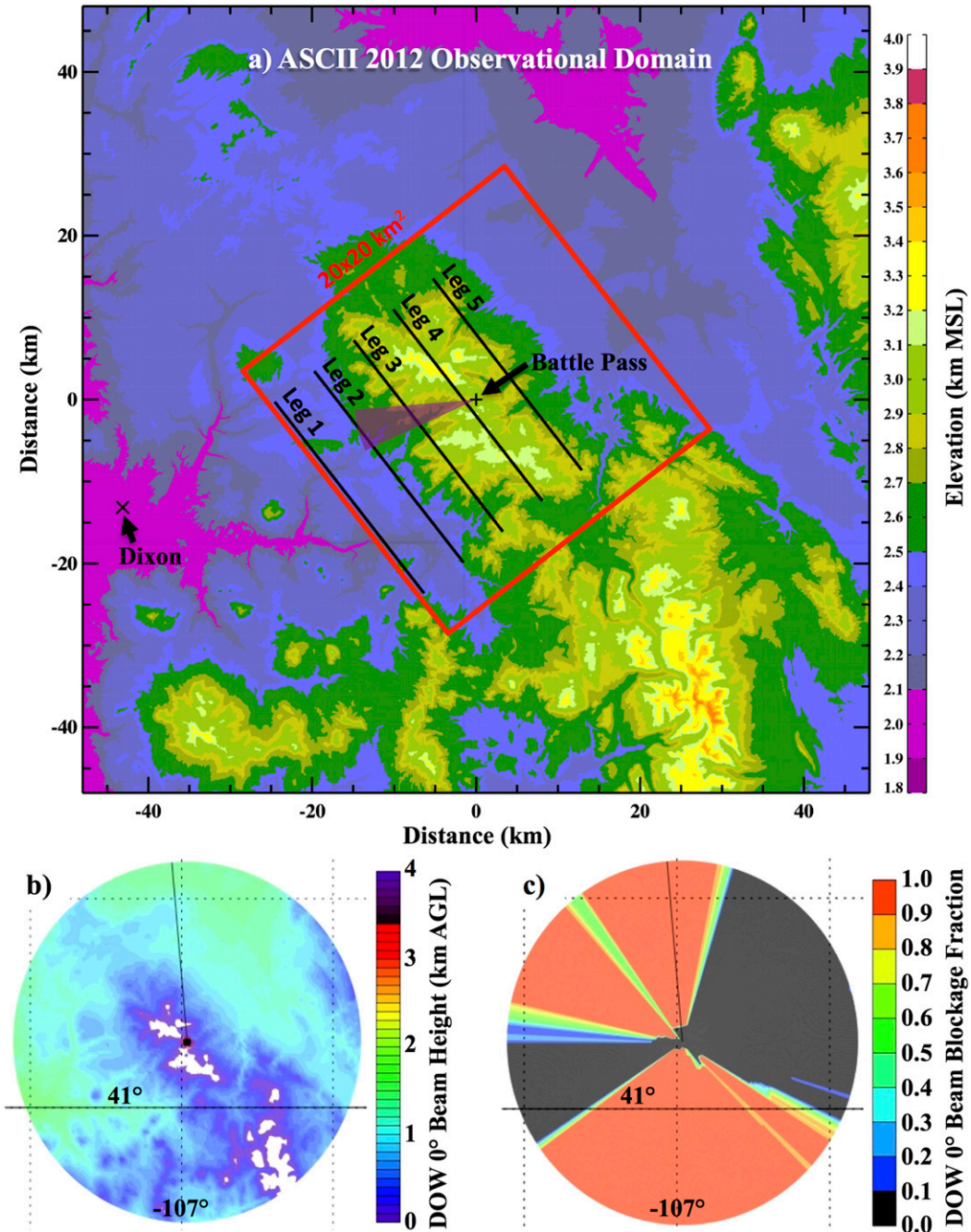


FIG. 1. (a) The observational domain (target area) for the ASCII 2012 field project plotted with 30-m resolution elevation data from the U.S. Geological Society (USGS) National Elevation Dataset (NED). Dixon (indicated by a cross) and Battle Pass (indicated by a plus sign) are labeled along with the UWKA ladder-pattern flight legs 1–5. The $20 \times 20 \text{ km}^2$ region centered at Battle Pass and rotated with the mean axis of the Sierra Madre Range is also overlaid with a red box, which is the analysis region used in the Hovmöller diagram in Fig. 2. The purple wedge starting from the DOW location at Battle Pass indicates the range of targeted DOW RHI azimuths used to calculate median profiles of Z and Z_{DR} (Fig. 7). (b) The DOW radar beam height (km AGL) calculated for an elevation scan of 0° . (c) The calculated fraction of the DOW radar beam that is blocked for a 0° elevation scan, where a fraction of 0.0 (1.0) indicates no (complete) beam blockage.

addition, Z_{DR} calibration scans were performed at 85° and 89° , followed by six range–height indicator (RHI) scans. Three RHI scans faced downwind and three faced upwind with the center RHI scan aligned with the mean wind direction during that time. A full three-dimensional radar volume was collected every 10 min. Significant beam blockage prevented reliable radar observations below 6° elevation scans to the north and south of Battle Pass (Figs. 1b,c).

Ground clutter and multipath scattering were removed from the PPI data using a fuzzy logic algorithm adapted from Gourley et al. (2007). The algorithm separates measurements contaminated by ground clutter and clear air from measurements of snow using dual-polarimetric variables Z_{DR} and ρ_{HV} and texture fields of Z_{DR} , Φ_{DP} , and ρ_{HV} . Bias corrections for Z_{DR} were first applied using the available calibration scans. The decluttered and quality-controlled polar-coordinate data were then interpolated onto a three-dimensional Cartesian grid using the National Center for Atmospheric Research (NCAR) Radx2-Grid software.¹ A horizontal grid spacing of 200 m was used (approximately three data points per horizontal grid cell). A vertical grid resolution of 250 m was determined by the tangent of the mean elevation angle between two consecutive beams at a half-distance of 30 km. The 30-km limit corresponds to the approximate distance between the foothills and Battle Pass. The maximum echo top never exceeded 10 km MSL, which was used as the upper boundary of the Cartesian grid.

2) MICRO RAIN RADAR

A vertically pointing Ka-band (continuous wave mode at 24.23 GHz) METEK Micro Rain Radar (MRR) was deployed at Battle Pass. Vertical profiles of reflectivity, Doppler velocity, and spectral width were averaged over 1-min intervals with a vertical resolution of 200 m in 31 range gates (up to 9.4 km MSL). Raw Doppler velocities from 0.95 to 12.195 m s^{-1} are recorded by assuming only downward motion, which is the sum of the vertical air motion and particle fall speeds. A Doppler spectra postprocessing technique created by Maahn and Kollias (2012) was implemented on the MRR data to improve sensitivity for snow and dealias Doppler velocities so that upward (positive Doppler velocity) and downward (negative Doppler velocity) motions can be distinguished within $\pm 12 \text{ m s}^{-1}$. The first two range gates were considered unreliable and were removed in this postprocessing. This makes the closest

reliable range gate for the Battle Pass MRR at 3.6 km MSL. MRRs have been used previously in various locations to monitor vertical precipitation structures (e.g., Löffler-Mang et al. 1999; Peters et al. 2002, 2005; Rollenbeck et al. 2007; Tokay et al. 2009; Trivej and Stevens 2010).

3) W-BAND WYOMING CLOUD RADAR

The 94.92-GHz (W-band) Doppler Wyoming Cloud Radar (WCR) was flown aboard the University of Wyoming King Air (UWKA) aircraft along with in situ cloud physics instruments. The WCR consisted of three antennas oriented up, down, and down-fore with beam widths of 0.7° , 0.5° , and 0.6° , respectively. A PRF of 20 kHz and a pulse width of 250 ns were used, resulting in a range resolution of 37.5 m. More details of the WCR system can be found in Wang et al. (2012) and references within. A schematic of the up, down, and down-fore radar beam configuration can be found in Fig. 2 of Geerts et al. (2006). Because of oversampling, a sampling interval of 15 m was achieved. This allowed very-high-resolution reflectivity and Doppler velocity observations above and below the aircraft flight level. Attenuation of the radar beam is assumed to be minimal due to the low Z observed in snowfall and the low amounts of liquid water observed during the case analyzed. A radar blind zone of 100 m above and below the aircraft flight level limited radar observations in the immediate vicinity of the aircraft. Postprocessing of WCR data included removing aircraft motion and horizontal wind velocity contamination from the Doppler velocity fields and correcting Z for range from the aircraft.

In situ cloud physics measurements of LWC from the UWKA flight path were obtained by the Droplet Measurement Technologies, Inc. (DMT) Cloud Droplet Probe (CDP), and ice particle concentrations for diameters between $62.5 \mu\text{m}$ and 2.5 mm were measured using the fast Optical Array Probe–2D Cloud (OAP-2DC) instrument (Wang et al. 2012). Vertical air motion, air temperature, and mixing ratio were measured by additional standard UWKA instrumentation.² A MacCready turbulence meter (MacCready 1964) aboard the UWKA allowed an in situ calculation of eddy dissipation rate (EDR), the cube root of the rate of dissipation of the turbulent kinetic energy and an indication of the strength of turbulence.

As indicated in Fig. 1a, the UWKA flew ladder patterns at ~ 4 km MSL consisting of five ladder legs parallel to the Sierra Madre Range. Ladder legs 1–3 were

¹ See http://www.ral.ucar.edu/projects/titan/docs/radial_formats/radx.html.

² See <http://www.atmos.uwyo.edu/uwka/index.shtml>.

upwind of the mountain crest, ladder leg 4 was along the mountain crest, and ladder leg 5 was immediately downwind of the mountain crest (Fig. 1a). Cross-barrier flight legs oriented parallel to the mean wind direction were flown during the ASCII project; however, no cross-barrier flight legs were flown during the analysis period presented in this paper.

b. Atmospheric profilers

The Mobile GPS Advanced Upper-Air Sounding balloon rawinsonde system (MGAUS³) was set up 45 km upwind from Battle Pass at Dixon Airport (hereafter referred to as Dixon; Fig. 1a). MGAUS soundings measured vertical profiles of humidity, temperature, and winds with high vertical resolution (1–5 m) in the upwind atmospheric environment every 1–2 h.

A Radiometrics Corporation passive microwave radiometer was deployed at Battle Pass and provided integrated liquid water (ILW) and integrated water vapor (IWV) measurements along with vertical profiles of temperature, humidity, LWC, and water vapor density for the mountain crest environment. The radiometer measures microwave emission at 22–30 GHz (water vapor absorption band) and 51–59 GHz (oxygen absorption band) as well as infrared emission at 9.6–11.5 μm . The zenith-pointing antenna has beam widths of 6° (22–30 GHz) and 2.5° (51–59 GHz). Vertical profiles of temperature and relative humidity were derived using a neural network algorithm (Solheim et al. 1998a,b). The algorithm, based on a radiative transfer model (Rosenkranz 1998), was trained on a 5-yr radiosonde climatology. Observations were integrated over 0.2 s, leading to a temperature resolution of 0.25 K. These measurements allow us to monitor atmospheric temperature and moisture changes above the terrain with higher temporal resolution than the MGAUS soundings.

c. Surface *in situ* instruments

1) PARSIVEL DISDROMETER AND SNOW CRYSTAL PHOTOGRAPHY

The laser-optical Particle Size and Velocity (PARSIVEL) disdrometer was installed in a forest opening at Battle Pass to measure *in situ* snow particle characteristics. The location was chosen to shield the instrument from strong winds that occur at the mountain pass and significantly influence measurement quality (Battaglia et al. 2010; Friedrich et al. 2013). The PARSIVEL disdrometer uses a laser beam to detect individual particle diameters and fall speeds, which allows a particle size and fall

velocity distribution to be created. Particle diameters are detectable between 0.25 and 25 mm and fall velocities between 0.2 and 20 m s^{-1} across 30×30 useable bins. Particle counts across these diameter and fall velocity bins are measured by the PARSIVEL every 10 s. Because of the complicated shapes of snow particles, reliable snow particle size and velocity observations are a challenge (Battaglia et al. 2010). Because of issues with border effects and multiple particle counts for a single snowflake, observations in size bins <1 mm were removed in the analysis. More reliable fall velocity measurements are retrieved for snow particles 1–10 mm in diameter, which are the particles of focus for this paper. Raw particle counts were used to compute normalized particle concentrations per volume ($\text{m}^{-3} \text{mm}^{-1}$). These normalized concentrations were then used to compute time series of total particle concentration and snowfall rate using the bulk snow density relation determined by Brandes et al. (2007).

Snow crystal photographs were taken on a black background every 10–15 min during intensive observational periods (IOPs) using a hand-held camera. These photographs allow visual determination of ice crystal habits and the degree of riming or aggregation for individual snow particles, which will be used to infer microphysical processes occurring within the overlying clouds.

2) SURFACE PRECIPITATION GAUGES AND WEATHER STATIONS

A Geonor all-weather precipitation gauge was installed at Battle Pass, which allowed *in situ* liquid-equivalent precipitation accumulation measurements. Although many other precipitation gauges were present at Battle Pass, the Geonor gauge was heated and thus provided the most reliable precipitation accumulations in snowfall. Storm-total precipitation accumulations and rates were calculated from these observations.

Surface weather observations were recorded at Dixon and Battle Pass, including temperature, pressure, relative humidity, wind speed, and wind direction. Measurements at Battle Pass were taken through a mesonet ~ 10 m above the surface on the mast of the DOW truck. Observations at Dixon were taken through NCAR's MGAUS surface weather station at ~ 1 –2 m above the surface.

3. Case overview

On 16 January 2012 (ASCII IOP2), widespread snowfall was observed throughout the target area between 1700 and 2130 UTC during and following the passage of a baroclinic front (Fig. 2). Many of the ASCII IOPs collected data during shallow storms with abundant LWC, largely because these conditions are prime for ground-based cloud seeding, which was the focus of

³ See <http://www.eol.ucar.edu/rtf/facilities/gaus/gaus.html>.

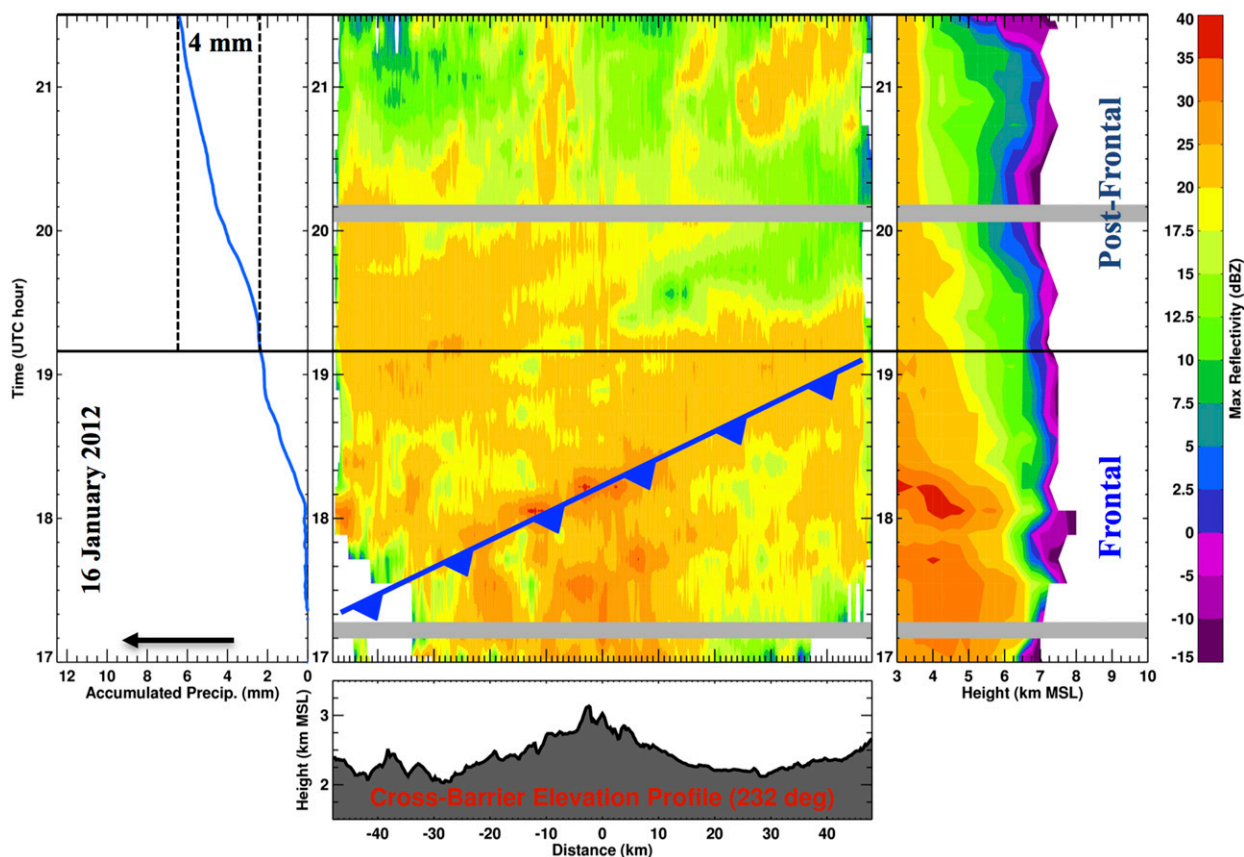


FIG. 2. (center) A Hovmöller diagram of maximum Z observed by the DOW radar above 3 km MSL, (left) accumulated surface precipitation from the Geonor precipitation gauge at Battle Pass, and (right) maximum Z observed by the DOW radar with height and time, for 1700–2130 UTC 16 Jan 2012 (IOP2). This period encompasses the baroclinic frontal passage and postfrontal stratiform precipitation that occurred during IOP2. The maximum Z for each x grid point in the Hovmöller diagram is computed within $y = \pm 20$ km, and the maximum Z with height is computed within the 20×20 km² region shown in Fig. 1a for each Cartesian-gridded DOW radar volume. The Cartesian-gridded DOW radar volumes used in this figure were rotated with the mean Sierra Madre Range axis so that the positive (negative) x axis is oriented at 52° (232°) from north, which is roughly perpendicular to the Sierra Madre barrier. The gray blocks in the center and right are time periods when no DOW radar data were available. The elevation profile along this azimuth, with the DOW location at Battle Pass at $x = 0$ km, is shown below the Hovmöller diagram.

the field project. Thus, IOP2 allows purely natural snow growth processes to be analyzed within a deep precipitation system associated with a baroclinic frontal passage. This period of IOP2 was chosen for analysis because the DOW observed a consistent deep precipitation layer (echo tops at 7–8 km MSL) with a moderate 6.5 mm of liquid-equivalent precipitation accumulating at Battle Pass (Fig. 2). Closer inspection of the precipitation accumulation at Battle Pass (Fig. 2) indicates two distinct periods of accumulation. A surface cold front, reaching up to 3.5 km MSL above Dixon by 2015 UTC (Fig. 3), moved over Dixon (Battle Pass) around 1720 UTC (1810 UTC) and exited the target region by 1910 UTC (Fig. 2). The front is evident by a band of high reflectivity ($Z > 35$ dBZ) observed by the DOW radar (Fig. 2), rapid snowfall accumulation at

Battle Pass between 1800 and 1900 UTC (2.7 mm h^{-1} ; Fig. 2), a sharp drop in surface temperatures at Battle Pass and Dixon ($6^\circ\text{--}7^\circ\text{C}$ by 2130 UTC; Fig. 4a), a 15 m s^{-1} spike in wind speed at Dixon and a sharp drop ($\sim 10 \text{ m s}^{-1}$) in wind speeds at Battle Pass (Fig. 4b), a sharp shift in wind direction at Dixon from south-southwest to northwest (Fig. 4c), a rapid increase in relative humidity from 60% to 85% at Dixon (Fig. 4f), and spikes in ILW (0.54 mm; Fig. 4e) and IWV (0.53 cm; Fig. 4g). We designate the period 1700–1910 UTC as “frontal” because the baroclinic front was responsible for generating precipitation over the ASCII target region during this time. The atmosphere was from moist neutral to moist unstable up to 5.5 km MSL prior to the front (Figs. 3 and 4d) with strong cross-barrier low-level winds ($10\text{--}25 \text{ m s}^{-1}$; Figs. 3 and 4b). The passage of the

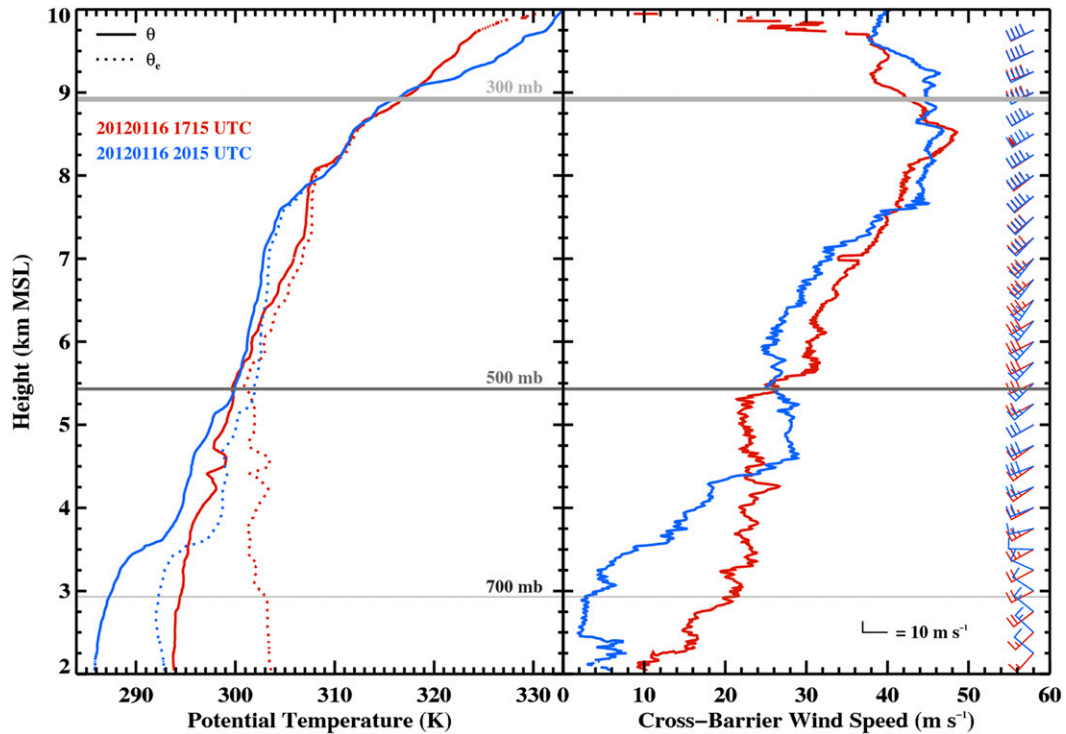


FIG. 3. MGAUS soundings launched from Dixon are plotted for 1715 (red) and 2015 UTC (blue) 16 Jan 2012. These times show the pre- and postfrontal environment during IOP2, respectively. (left) Potential temperature θ (solid line) and equivalent potential temperature θ_e (dotted line); (right) computed cross-barrier wind speed. Median wind speed and direction are also plotted as a wind barb every 0.25 km MSL (flag = 50 m s⁻¹; full barb = 10 m s⁻¹; half barb = 5 m s⁻¹). The cross-barrier wind speed was computed as the component of the observed wind in a 232° wind direction. Horizontal gray lines denote the range of heights at which the 300- (light gray), 500- (medium gray), and 700-mb (dark gray) pressure levels were located in the soundings shown.

cold front stabilized the atmosphere (Fig. 4d) and decoupled the boundary layer from the upper air with an inversion that developed near 3.5 km MSL by 2015 UTC (Fig. 3). This inversion separated postfrontal northwesterly (along barrier) slightly moist unstable flow from strong (10–30 m s⁻¹) southwesterly (cross barrier) stable flow above. Note that the northwesterly flow is part of the low-level postfrontal air mass and not a result of deflected airflow. The surface-based calculation of moist Froude number (Fr_m) following the frontal passage stayed relatively steady near 1, indicating wave motions over the mountain were likely. The period from 1910 to 2130 UTC is designated as “post frontal” and is the main focus of the following analysis due to the shear instability that set up during this time.

4. Precipitation processes indicated by surface observations and radar

During the postfrontal period between 1910 and 2130 UTC 16 January 2012, deep, widespread stratiform clouds and precipitation dominated the ASCII target

region with maximum Z of 5–25 dBZ observed by the DOW radar (Figs. 2 and 5). A total of 4 mm of precipitation accumulated at Battle Pass during this time with decreasing intensity (1.3–2.9 mm h⁻¹; Fig. 2). At the beginning of this period (1910–2000 UTC), higher reflectivity (maximum $Z > 20$ dBZ) was observed from ~50 km upwind to Battle Pass. This enhanced precipitation was advected from the southwest by an approaching midlevel cross-barrier jet (see section 5). Later (2000–2130 UTC), higher Z only occurred 5–15 km upwind of Battle Pass. These isolated areas of higher Z (18–25 dBZ) after 2000 UTC were generated mainly below 4 km, as shown in Fig. 2 and the individual DOW radar volume at 2023 UTC (Fig. 6).

To further investigate precipitation processes during this postfrontal period, we analyze vertical profiles of median Z and Z_{DR} from DOW RHI scans (best available RHI scan every 10 min; Fig. 7). Median profiles were derived from data collected over a 15-km region immediately upwind from Battle Pass (245°–265° azimuths; Fig. 1a). At upper levels between 5.5 and 7 km MSL, median profiles of Z and Z_{DR} rapidly increased

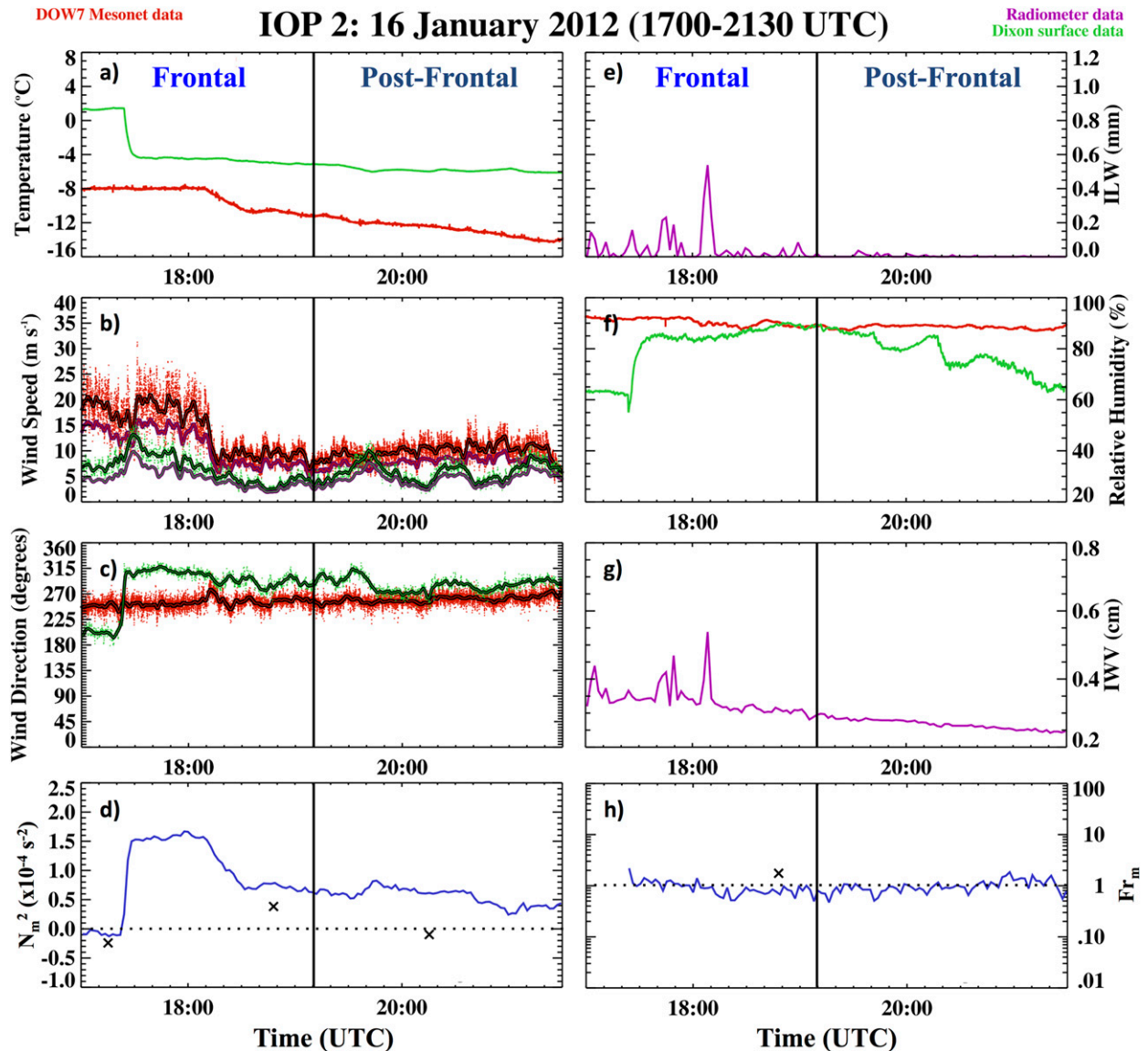


FIG. 4. Surface weather observations, vertically integrated liquid water and water vapor, and surface- and sounding-based stability parameters are plotted between 1700 and 2130 UTC 16 Jan 2012 (IOP2). (a) Air temperature, (b) wind speed, (c) wind direction, and (f) relative humidity observations are plotted for Dixon (green) and Battle Pass (red). Raw (dots) and 60-s averaged (solid line) surface wind speed observations (black line border) at Dixon (green) and Battle Pass (red) as well as computed cross-barrier wind components (purple line border) are plotted in (b). Also shown are (e) ILW and (g) IWV observations from the microwave radiometer at Battle Pass and computed (d) moist squared Brunt-Väisälä frequency N_m^2 and (h) Fr_m . The blue lines in (d) and (h) are calculated using surface observations from Dixon and Battle Pass, and the black crosses are calculated using MGAUS soundings from Dixon. The N_m^2 and Fr_m values were computed using observations at the two elevations corresponding to Dixon (1980 m MSL) and Battle Pass (3030 m MSL). The separation between moist stable ($N_m^2 > 0$) and moist unstable conditions ($N_m^2 < 0$) is denoted by a dotted black line at $N_m^2 = 0$ in (d). The transition between blocked flow ($Fr_m < 1$) and unblocked flow ($Fr_m > 1$) is separated by a dotted black line at $Fr_m = 1$ in (h). A vertical black line separates the frontal and postfrontal periods mentioned in the paper, similar to Fig. 2.

with decreasing height by 10–15 dBZ km⁻¹ (Fig. 7a) and 0.5–1.5 dB km⁻¹ (Fig. 7b), respectively. Higher median Z was observed in this layer around 1930 UTC (up to 4 dBZ), suggesting that upper-level snow growth was enhanced during this time. Temperatures in this layer

ranged between -28° and -40°C (Fig. 7). Studies have shown that pristine platelike snow crystals (Bailey and Hallett 2009) grow through water vapor deposition in this temperature region near cloud tops of stratiform precipitation with low reflectivity ($-10 < Z < 10$ dBZ)

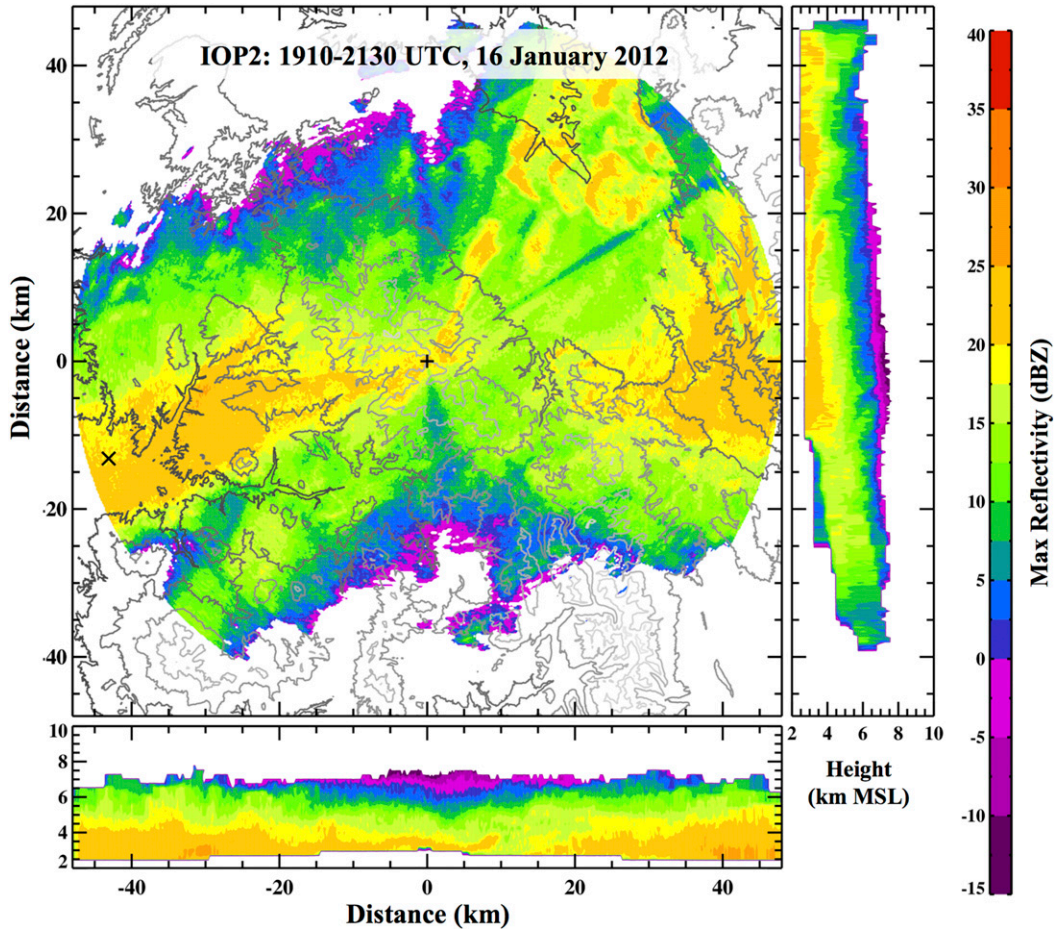


FIG. 5. Maximum Z observed by the DOW radar above 2 km MSL is plotted for the postfrontal period between 1910 and 2130 UTC 16 Jan 2012 (IOP2). (top left) USGS NED terrain elevation is overlaid on the maximum Z . (bottom) Maximum Z at each (x, z) grid point within $y = \pm 20$ km and (top right) maximum Z at each (y, z) grid point within $x = \pm 20$ km is plotted. The DOW location at Battle Pass is labeled as a black plus sign, and Dixon is marked with a black cross. Elevation contours are at 2.1, 2.4, 2.7, 3.0, 3.3, and 3.6 km MSL and are colored dark gray at low elevations (2.1 km MSL) and light gray at high elevations (3.6 km MSL). See text for further details.

and positive Z_{DR} between 0 and 2 dB (Ryzhkov and Zrnić 1998; Moissev et al. 2009; Kennedy and Rutledge 2011; Bechini et al. 2013; Schneebeli et al. 2013).

At midlevels between 4 and 5.5 km MSL, Z_{DR} increased less rapidly ($< 0.5 \text{ dB km}^{-1}$) and became fairly constant with height between 1.5 and 2 dB (Fig. 7b). The Z_{DR} contoured frequency by altitude diagram (CFAD; not shown) shows that 30%–50% of the observed Z_{DR} was between 1.5 and 2 dB in this layer. Median Z generally continued to increase (up to 15 dBZ) with decreasing height at varying rates with time in this midlevel layer ($1\text{--}20 \text{ dBZ km}^{-1}$; Fig. 7a). Temperatures in this layer ranged between -18° and -28°C (Fig. 7). These observations indicate pristine horizontally oriented snow crystals likely grew in size without changing their shape in this layer. Also note that the overall Z and Z_{DR} in this

layer decreases over time after 1930 UTC (Fig. 7), indicating that snow particles likely became smaller with less oblate shapes between 1930 and 2130 UTC.

At low levels between 3 and 4 km MSL, reflectivity generally increased slightly with decreasing height ($0\text{--}10 \text{ dBZ km}^{-1}$), but rapid increases in Z ($> 20 \text{ dBZ km}^{-1}$) were observed at the beginning (before 1930 UTC) and end (around 2130 UTC) of this analysis period (Fig. 7a). Note that Z_{DR} generally remained constant or decreased with decreasing height in this layer (-0.1 dB km^{-1} ; Fig. 7b), but Z_{DR} increased where rapid reflectivity increases occurred before 1930 UTC and around 2130 UTC. Temperatures in this layer ranged from -14° to -18°C (Fig. 7). Localized positive Z_{DR} and specific differential phase K_{DP} enhancements in areas with temperatures near -15°C are often associated with rapid

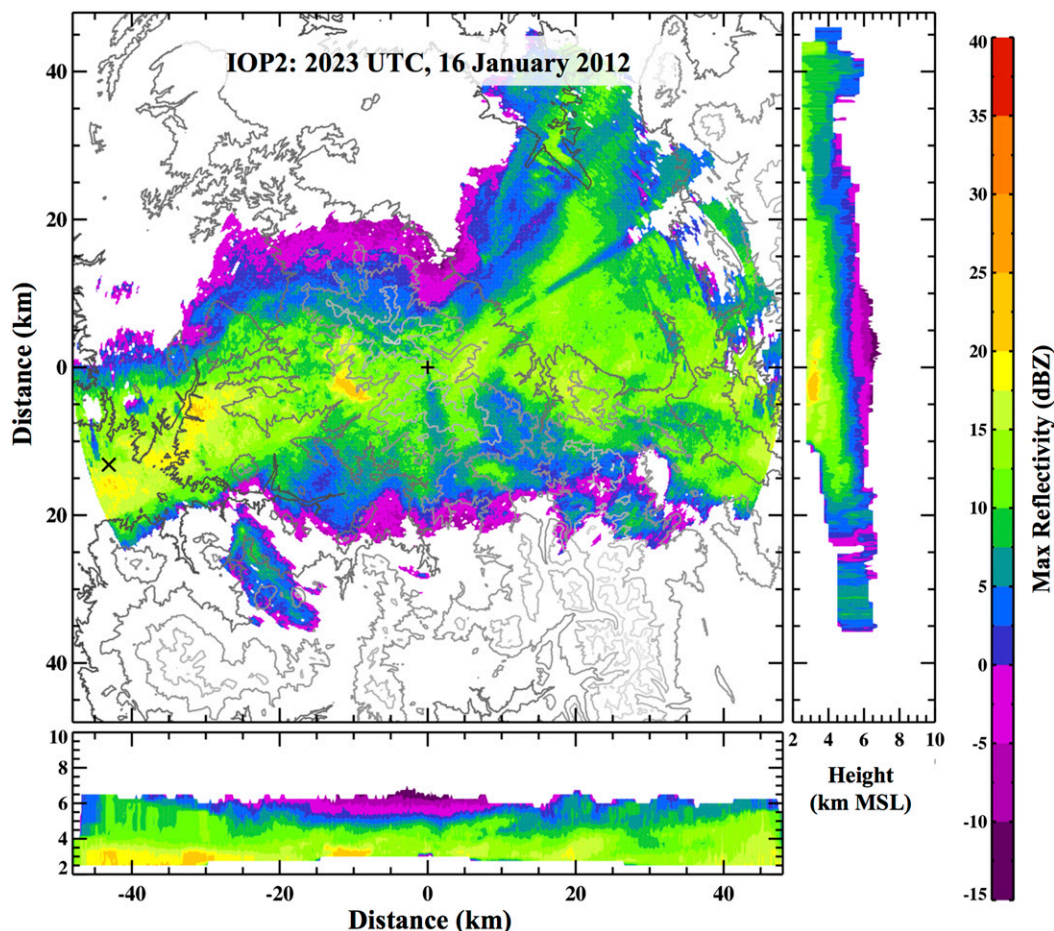


FIG. 6. As in Fig. 5, but for a single Cartesian-gridded DOW radar volume at 2023 UTC 16 Jan 2012 (IOP2).

dendritic growth (Hogan et al. 2002; Andrić et al. 2010; Kennedy and Rutledge 2011; Andrić et al. 2013; Bechini et al. 2013). The positive K_{DP} signature usually associated with rapid dendritic growth cannot be verified in this case because Φ_{DP} measurements became unreliable during this period.

In situ snow particle observations at the Battle Pass surface (~ 3 km MSL) can be used to verify microphysical growth mechanisms indicated by the DOW radar. Dendritic growth before 1930 UTC is supported by surface snow crystal photographs taken at 1920 UTC at Battle Pass, which show the presence of dendrites, stellar crystals, and large dendritic aggregates (Fig. 8a, left). PARSIVEL observations at Battle Pass before 1930 UTC show an increase in total particle concentration (from 300 to 2000 m^{-3} ; Fig. 8b), increased snowfall rate (from 0.3 to 2 $mm h^{-1}$; Fig. 8d), and the presence of large particles (diameter $d > 5$ mm; Fig. 8c), indicative of the observed large dendritic aggregates. After 2000 UTC, smaller unrimed plates, sectored

plates, capped columns, and irregular polycrystalline platelike crystals were observed during the remainder of the analysis period (Figs. 8a, center and right). PARSIVEL observations support snow crystal photographs indicating that smaller particle diameters ($d < 5$ mm) were observed after 1930 UTC (Fig. 8c). However, total particle concentrations and snowfall rates remained elevated at $\sim 1000 m^{-3}$ and $\sim 1 mm h^{-1}$ until 2107 UTC (Figs. 8b,d). No clear photographs of fernlike dendritic crystals were observed at the surface around 2130 UTC, but stellar dendrites were captured (Fig. 8a, right). PARSIVEL observations show the return of larger aggregates ($d > 5$ mm; Fig. 8c) and increased total particle concentrations (2500 m^{-3} ; Fig. 8b) and snowfall rates (2 $mm h^{-1}$; Fig. 8d) around 2130 UTC. Note that the presence of larger aggregates at the Battle Pass surface after 2130 UTC seem to be collocated with the dendritic growth signatures indicated by the DOW radar within 1 km above the Battle Pass surface. This is expected because dendrites are more

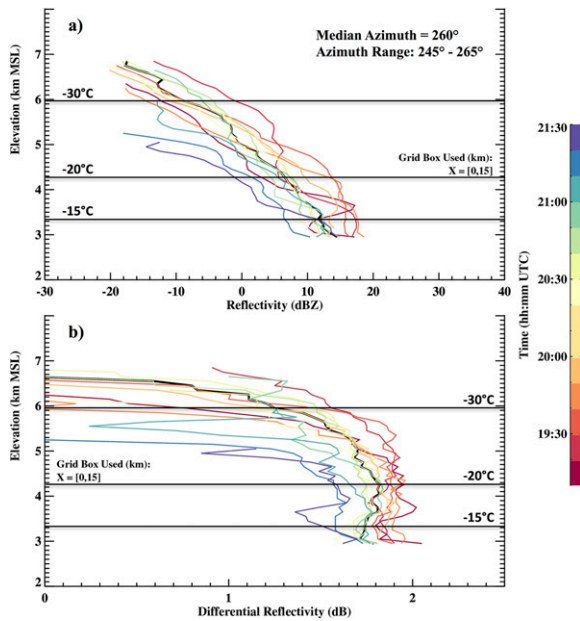


FIG. 7. Median profiles of (a) Z and (b) Z_{DR} calculated from upwind DOW radar RHI scans every ~ 10 min between 1910 and 2130 UTC 16 Jan 2012 (IOP2). Each median profile is calculated within a horizontal distance of 0–15 km from the DOW radar. The color-coded times of each median profile can be identified by the color bar. The overall median profile over this time period is plotted as the thick black line. The median targeted RHI azimuth and azimuth range during 1910–2130 UTC is displayed in (a) and Fig. 1a for reference. The mean heights of the -15° , -20° , and -30° temperature levels observed by the radiometer at Battle Pass are overlaid and labeled. Note that no RHI scans were available between 2000 and 2010 UTC.

susceptible to aggregation due to mechanical interlocking (e.g., Rauber 1987). Dendritic aggregates have been observed and modeled to have low Z_{DR} (~ 0 dB) due to their quasi-spherical shapes and tendency to tumble (Ryzhkov and Zrnić 1998; Andrić et al. 2010; Kennedy and Rutledge 2011; Andrić et al. 2013). The presence of aggregates may explain the relative minima in Z_{DR} below 4 km MSL before 1930 UTC and around 2130 UTC (Fig. 7b). However, the still relatively high median Z_{DR} within these minima (1.35–1.8 dB; Fig. 7b), as well as the small concentration of particles having $d > 5$ mm (up to $200 \text{ m}^{-3} \text{ mm}^{-1}$; Fig. 8c), indicates that large aggregates did not dominate the DOW radar signal. Rather, the horizontally oriented pristine dendrites and stellar crystals present during these times dominated. The relatively low height of the dendritic growth layer near -15°C (within 1 km above the Battle Pass surface) likely prevented substantial aggregation before reaching the Battle Pass surface.

The MRR at Battle Pass observed echo tops ($Z = \sim -5$ dBZ) up to 6 km MSL over the mountain crest with

an overall steady increase in median Z with decreasing height at a rate of 7 dBZ km^{-1} between 3.6 and 6 km MSL (Fig. 9a). This stratiform reflectivity profile is similar to the overall median Z observed by the DOW radar immediately upwind of Battle Pass ($\sim 8 \text{ dBZ km}^{-1}$) between 3 and 6.8 km MSL (Fig. 7a). The MRR-observed reflectivity profile over time (Fig. 10a) shows changes in precipitation with increased temporal resolution (1 min) compared to the DOW observations (10 min). MRR-observed echo top increased significantly between 1910 and 1930 UTC from 4.2 to 6 km MSL (Fig. 10a), indicating that upper-level precipitation growth was enhanced and advected over Battle Pass (Fig. 2) during this time. This agrees with the DOW-observed reflectivity profiles as median Z increased by 3–11 dBZ between 1915 and 1925 UTC above 4 km MSL (Fig. 7a). At low levels between 3.6 and 4 km MSL, MRR-observed reflectivity consistently increased rapidly with decreasing height ($12\text{--}25 \text{ dBZ km}^{-1}$) during this time (Fig. 10a). The DOW radar observed similar reflectivity increases in this layer before 1930 UTC (Fig. 7a). The highest reflectivities observed by the MRR ($20\text{--}25 \text{ dBZ}$) occurred in pockets below 4.5 km MSL between 1930 and 2015 UTC (Fig. 10a). This agrees with the DOW observations as median Z is highest and consistently above the overall median between 3.6 and 4.5 km MSL from 1930 to 2000 UTC (Fig. 7a). PARSIVEL observations at the Battle Pass surface also indicate that the heaviest snowfall rates occurred during this time ($1\text{--}4 \text{ mm h}^{-1}$; Fig. 8d). After 2015 UTC, MRR-observed Z generally decreased at all heights, but individual towering reflectivity enhancements were observed up to 6 km MSL between 2030 and 2100 UTC (Fig. 10a). After 2100 UTC, MRR echo top decreased steadily down to 4.6 km MSL.

5. Cross-barrier jet and plunging flow: Implications for microphysical processes

Vertical profiles of MRR-observed Doppler velocity show a distinct layer of enhanced downward motion (Doppler velocities $< -3 \text{ m s}^{-1}$) between 4.1 and 5.3 km MSL, with the strongest downward motion occurring between 2010 and 2120 UTC (Figs. 9b and 10b). This area of enhanced downward motion is collocated with a distinct cross-barrier jet that was observed by the DOW radar between 1920 and 2115 UTC (coinciding with the arrival of the advected upper-level reflectivity enhancement) and by the 2015 UTC upwind sounding (Fig. 3). Doppler radial velocity fields observed by the upwind (260° azimuth) and downwind (79° azimuth) DOW RHI scans at 2055 UTC (Fig. 11a) indicate this

a) Snow Crystal Photographs | 1910-2130 UTC, 16 January 2012 (IOP2)

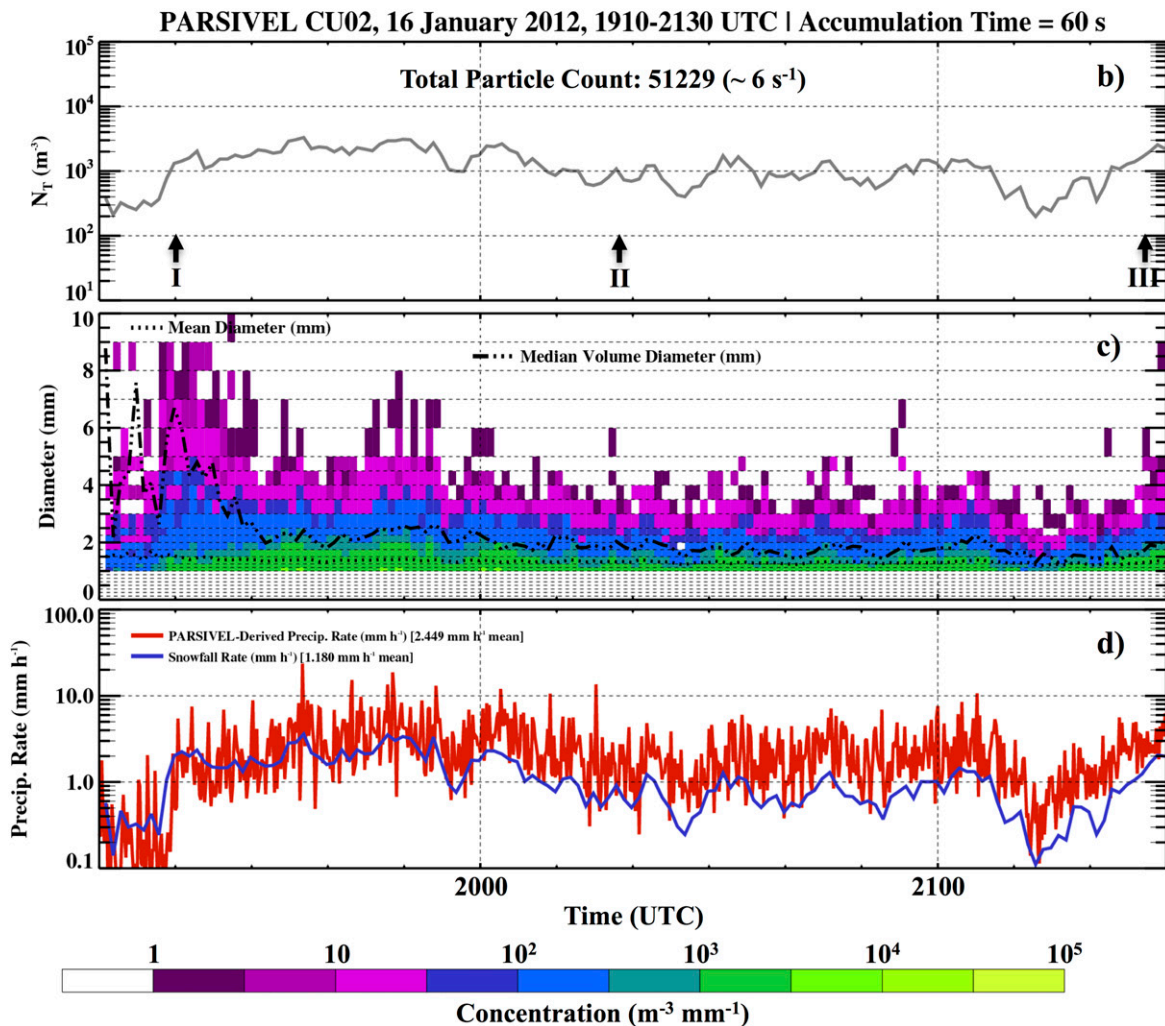
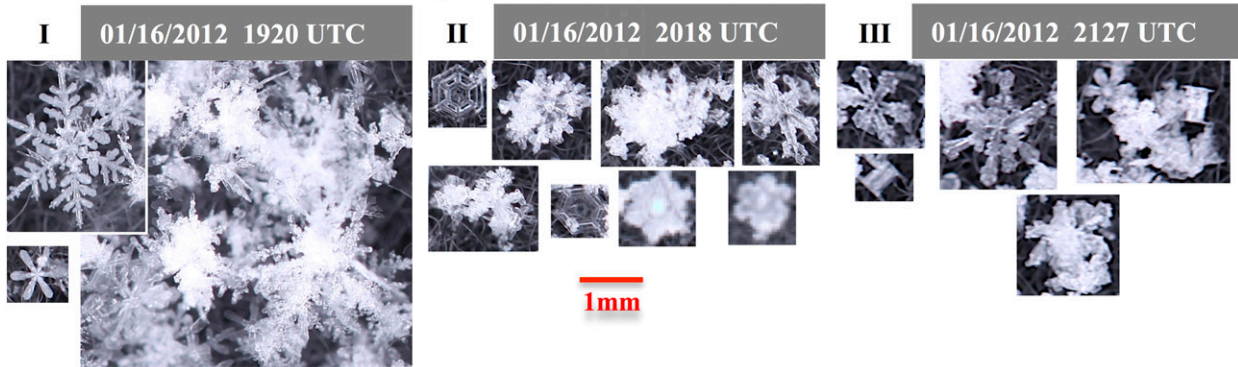


FIG. 8. (a) Snow crystal photographs taken on the surface of Battle Pass at (left; labeled “I”) 1920, (center; labeled “II”) 2018, and (right; labeled “III”) 2127 UTC 16 Jan 2012 (IOP2). Also, PARSIVEL disdrometer observations from Battle Pass between 1910 and 2130 UTC 16 Jan 2012 (IOP2) are plotted, including (b) total particle concentration, (c) normalized particle concentrations per diameter bin (see concentration color bar), and (d) raw PARSIVEL-derived precipitation rates and calculated snowfall rates. The mean (median volume) particle diameter over time is plotted as a dotted (dash dotted) line in (c) as well. The total particle count observed by the PARSIVEL disdrometer during this time is labeled along with the mean number of observed particles per second in (b). The times when the snow crystal photographs were taken are indicated in (b). Note that all PARSIVEL observations with particle diameters less than 1 mm were removed from the dataset before calculating particle size distribution–derived parameters, but the raw PARSIVEL-derived precipitation rate takes into account all measured particles.

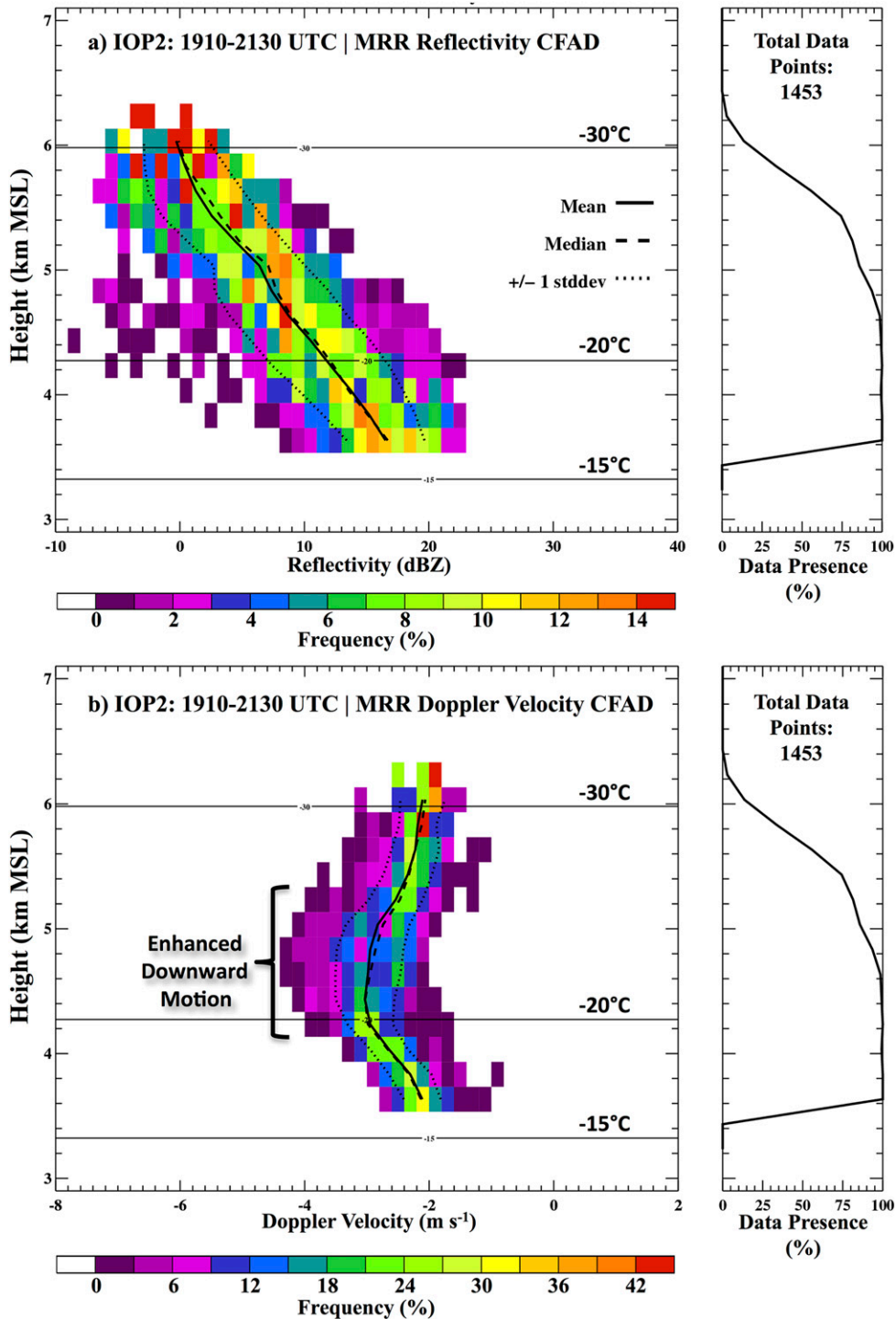


FIG. 9. (left) CFADs for (a) Z and (b) Doppler velocity observed by the vertically pointing MRR at Battle Pass during 1910–2130 UTC 16 Jan 2012 (IOP2). Frequency is a function of height, so summing the frequencies along a specific height level will result in 100%. Note that the frequency scale changes between the Z and Doppler velocity CFADs. The mean temperature heights during 1910–2130 UTC 16 Jan 2012 (IOP2) are labeled based on temperature profiles observed by the radiometer at Battle Pass. (right) The total number of MRR-observed Z and Doppler velocity observations and the data presence, the percentage of measurement times with data present in each height level during this time period, are shown. The mean, median, and plus/ minus one std dev of Z and Doppler velocity for each height are plotted in the respective CFADs. See text for further details.

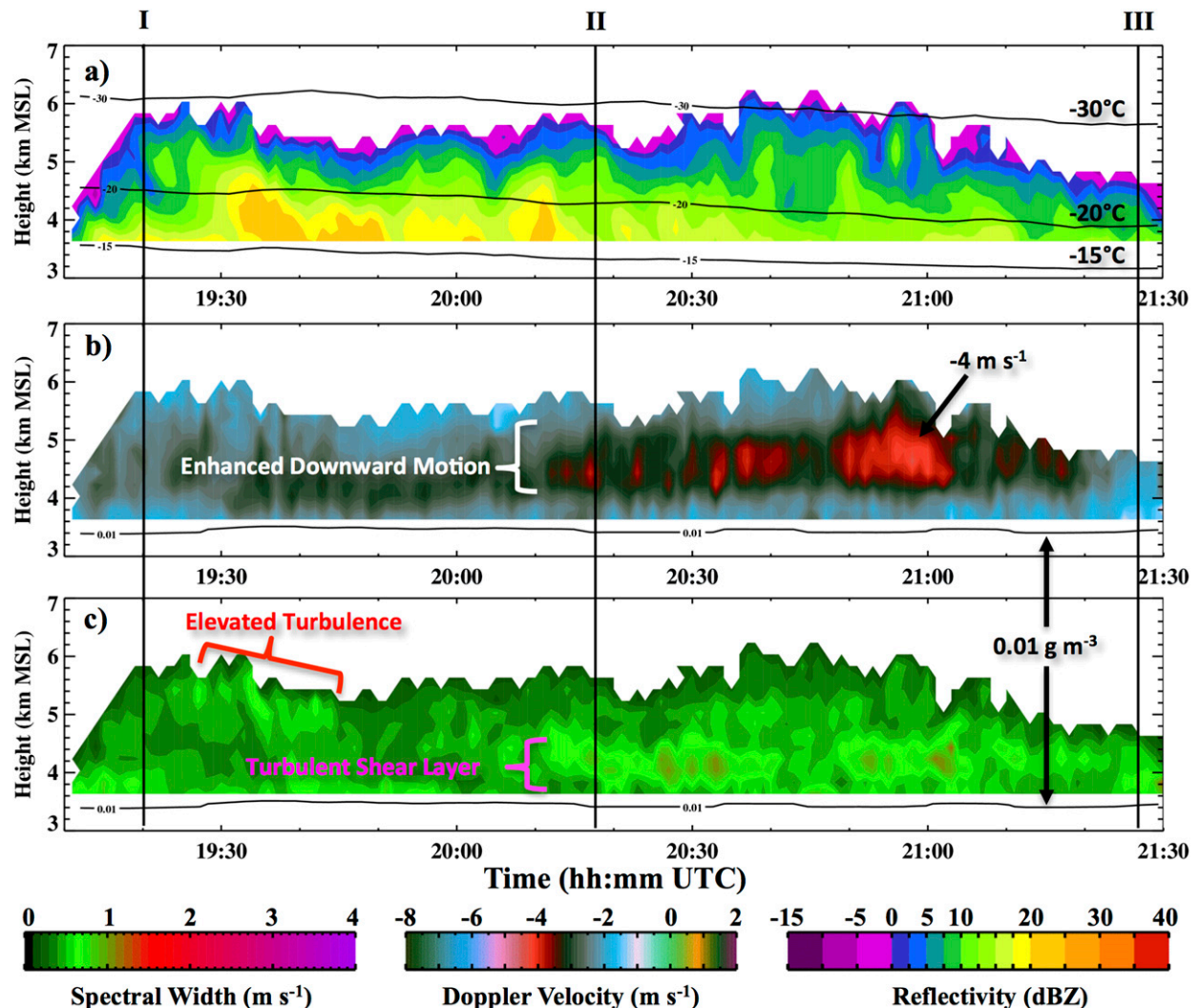


FIG. 10. Time–height profiles of (a) Z, (b) Doppler velocity, and (c) spectrum width observed by the MRR at Battle Pass during 1910–2130 UTC 16 Jan 2012 (IOP2). Radiometer-observed temperature levels (-30° , -20° , and -15°C) are overlaid in (a) and radiometer-observed LWC levels are overlaid in (b) and (c) as solid black lines. The times the snow crystal photographs (Fig. 8a) were taken are labeled as I, II, and III in the time–height plots of MRR data. Note that the MRR is vertically pointing, so Doppler velocities are positive for upward motion and negative for downward motion. See text for further details.

cross-barrier jet between 4 and 6 km MSL with maximum Doppler velocities of $25\text{--}30\text{ m s}^{-1}$. The calculated cross-barrier wind speed from the 2015 UTC sounding (Fig. 3) shows a relative enhancement indicative of a cross-barrier jet between 4.3 and 5.5 km MSL with maximum cross-barrier winds approaching 30 m s^{-1} near 4.6 km MSL.

Decreasing MRR-observed Doppler velocities can be related to an increase in downward air motion, an increase in particle fall velocity, or both. Negative Doppler velocities exceeding 3 m s^{-1} in magnitude are much higher than typical observed fall velocities of snow crystals ($<1.5\text{ m s}^{-1}$; Lamb and Verlinde 2011,

their Figs. 9.7 and 9.10) and aggregates ($<2\text{ m s}^{-1}$; Brandes et al. 2008). Since the precipitation analysis (section 4) indicates that pristine snow crystals dominated the reflectivity signal during this period, the enhanced downward motion observed by the MRR (Figs. 9b and 10b) can be related to an increase in downward air motion rather than an increase in particle fall speed. Strong downward motion within orographic flow, also referred to as plunging flow, has been observed and modeled in various orographic settings on the lee side of mountain barriers (e.g., Garvert et al. 2007; Smith et al. 2012; Saleeby et al. 2013; Geerts et al. 2015). Geerts et al. (2015) observed plunging flow in

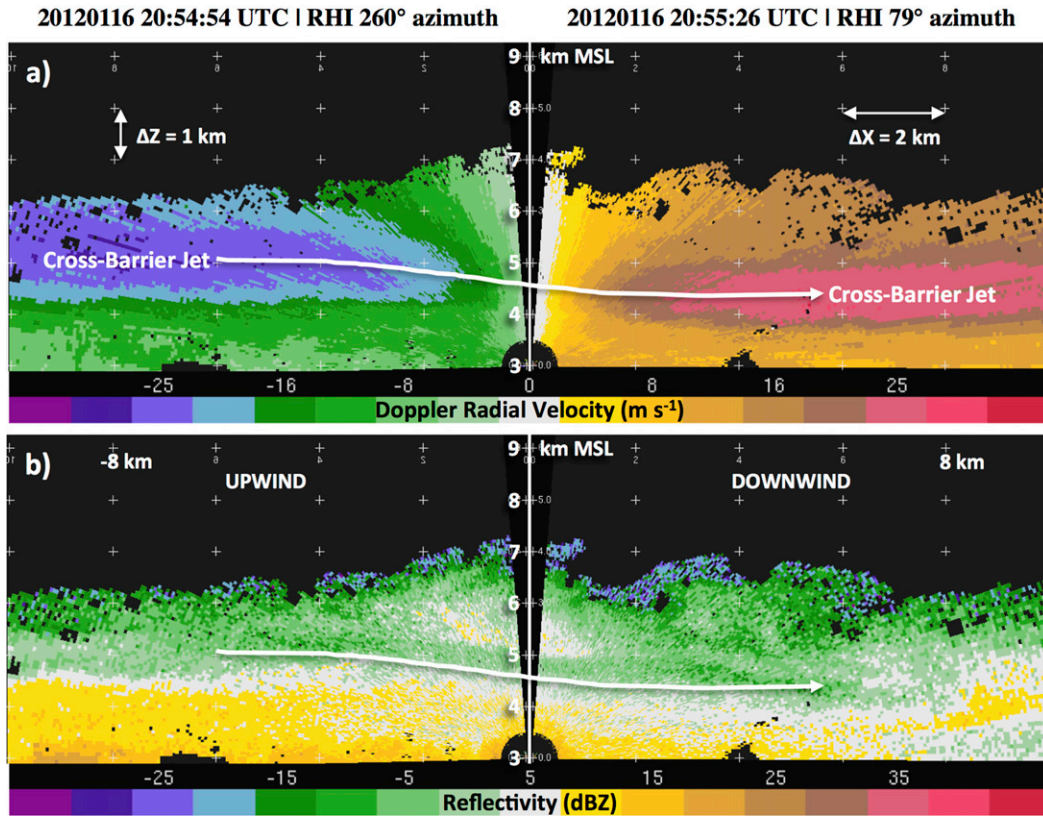


FIG. 11. (a) Doppler radial velocity and (b) Z observed by the DOW radar RHI scans at 2055 UTC 16 Jan 2012. Tick marks (plus signs) in (a) and (b) denote Cartesian heights and distances from the DOW radar, which are spaced every 1 km in height (Δz) and every 2 km in horizontal distance (Δx). The ± 8 -km horizontal distance tick marks are labeled in (b). The center of the cross-barrier jet is denoted with a white arrow in (a) and (b). Doppler dealiasing was performed on the Doppler velocity field using the Soloi radar software.

winter snowstorms over an adjacent mountain range in Wyoming, the Medicine Bow Range, using the WCR flown aboard the UWKA. They show that this plunging flow is characterized by strong downward air motion immediately downwind of the mountain crest, which causes snow to fall out rapidly and sublimate in the lee (typically within ~ 20 km from the crest for stratiform precipitation). They also observed low-level cross-barrier jets riding up and over the mountain, with the jet decreasing in height in the lee and sometimes accelerating. Leeward plunging flow is typically associated with a vertically propagating mountain wave centered at the mountain crest (Garvert et al. 2007; Geerts et al. 2015). Unfortunately no along-wind UWKA flights were flown during this period, so cross-barrier WCR-observed Z and Doppler vertical velocity transects similar to analysis in Geerts et al. (2015) are not available. However, plunging flow is indicated by the decrease in height of the maximum Doppler radial velocities as well as the decreasing height of the 5-dBZ reflectivity contour observed by

the DOW radar from upwind to downwind at 2055 UTC (denoted by the white line/arrow in Figs. 11a,b). At Battle Pass, the downward motion observed by the MRR did not reach the surface. It is not clear whether the decoupled boundary layer prevented the flow from reaching the surface or if plunging flow reached the surface farther downstream.

Plunging flow is important because it impacts the distribution and intensity of snowfall over the leeward mountain slope. Downward air motion is detrimental to precipitation growth because adiabatic motion favors warming and drying, and thus evaporation and sublimation (e.g., Saleeby et al. 2013). That means snow particles that grow upwind of the mountain and are advected into the lee encounter either no further particle growth or sublimation, thus favoring decreased surface precipitation in the lee. This was observed by the DOW radar as a decrease in median Z during this period from 20–30 km upwind to 10–20 km downwind of Battle Pass (Fig. 12). Below 4 km MSL, median Z remained above 10 dBZ for all upwind profiles and

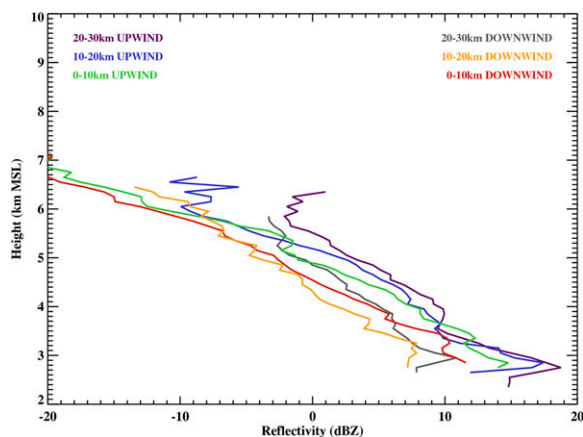


FIG. 12. Median profiles of Z are shown for cross-barrier transects from upwind-facing (245° – 265°) and downwind-facing (70° – 85°) DOW RHI scans during 1910–2130 UTC 16 Jan 2012. These transects are broken into six 10-km horizontal distances: from -30 to -20 km (upwind), $+20$ to $+30$ km (downwind), -20 to -10 km (upwind), $+10$ to $+20$ km (downwind), -10 to 0 km (upwind), and 0 to $+10$ km (downwind) from the DOW radar location at Battle Pass.

then decreased below 10 dBZ for all downwind profiles. A slight increase in median Z occurred at all levels between the 10–20- and 20–30-km downwind profiles (Fig. 12). This downwind increase in reflectivity can also be seen in the Hovmöller diagram (Hovmöller 1949) beyond 20 km downwind after 2030 UTC (Fig. 2) and indicates a return to orographic ascent and particle growth over the downwind Medicine Bow Range (Figs. 1 and 2).

6. Turbulent motion and implications for microphysical processes

An increase in spectrum width was observed by the MRR between 3.6 and 4.6 km MSL during the strongest plunging flow from 2010 to 2120 UTC (Fig. 10c). Increased spectrum width can be an indication of increased turbulence or fall speed diversity of falling precipitation particles. Because fall speeds of pristine ice crystals vary little with size (Locatelli and Hobbs 1974), turbulence dominated the spectrum width signal during this time period. The sharp decrease in cross-barrier wind speed below the jet maximum indicated by the 2015 UTC sounding within 3.25–4.6 km MSL (15 – 30 m s^{-1} km^{-1} ; Fig. 3), which is well above the 10 m s^{-1} km^{-1} threshold identified by HM05, and the Doppler radial velocity field in the DOW RHI scans at 2055 UTC (Fig. 11a) indicate that this turbulence was likely generated by shear. Backing of winds in this shear layer, from northwesterly within the decoupled boundary layer to

southwesterly above the inversion at 3.5 km MSL, partially contributed to this cross-barrier wind shear, but wind speeds also increased from 10 to 30 m s^{-1} between 3.25 and 4.5 km MSL (Fig. 3). Because the MRR is pointing vertically, this turbulent motion indicates rapidly fluctuating air motion, or updrafts and downdrafts. The MRR-observed Doppler velocity CFAD (Fig. 9b) and 1-min profiles (Fig. 10b) show mean downward motion in this turbulent shear layer (from -2 to -3 m s^{-1}), associated with the plunging flow above Battle Pass, but small-scale alternating fluctuations between -0.8 and -4.4 m s^{-1} were present. These fluctuations can be related to pockets of overturning cells with 1 – 2 m s^{-1} updrafts and downdrafts.

Along-barrier UWKA flight legs flown between 1925 and 1951 UTC indicate turbulence with updrafts up to 2 m s^{-1} within the shear layer between 3.6 and 4.7 km MSL that appears separate from a turbulent terrain-following boundary layer below 3.6 km MSL (Fig. 13). Note that the time of the UWKA along-barrier flights lies outside the time when the strongest plunging flow and shear-layer turbulence was identified over Battle Pass (2010–2120 UTC). However, because the synoptic system is progressing to the southeast during this time and the cross-barrier jet was identified as entering the target region with the advected upper-level reflectivity enhancement by 1920 UTC, the turbulent shear layer should appear to the northwest in the flight legs. This seems to be the case as turbulence within the shear layer is best observed by the WCR to the northwest in flight legs 3 and 4 (pink boxes in Figs. 13b,c). In situ vertical wind measurements from the UWKA also observed turbulent vertical air motions within ± 2 m s^{-1} at flight level (4 km MSL) throughout each flight leg (Fig. 13). To further quantify the turbulence observed by the UWKA, Fig. 14 plots the in situ eddy dissipation rate, the cube root of the rate of dissipation of the turbulent kinetic energy, measured by the MacCready turbulence meter (MacCready 1964) for the same flight legs shown in Fig. 13. Based on previous classifications (Strauss et al. 2015), EDR thresholds of 0.014, 0.050, 0.125, 0.220, 0.350, and 0.500 $\text{m}^{2/3} \text{s}^{-1}$ designate smooth-to-light, light, light-to-moderate, moderate, moderate-to-severe, and severe turbulence categories, respectively. It can be seen that the UWKA generally experienced greater-than-light turbulence for the majority of the along-barrier flight legs, with the strongest turbulence (moderate to severe) being observed within the turbulent shear layer identified by the pink box in leg 4 (Fig. 14). However, the turbulence observed within the shear layer by the WCR and UWKA in situ sensors seems to be subkilometer scale. Additionally, MRR-observed spectrum width within the shear layer during the UWKA flight times

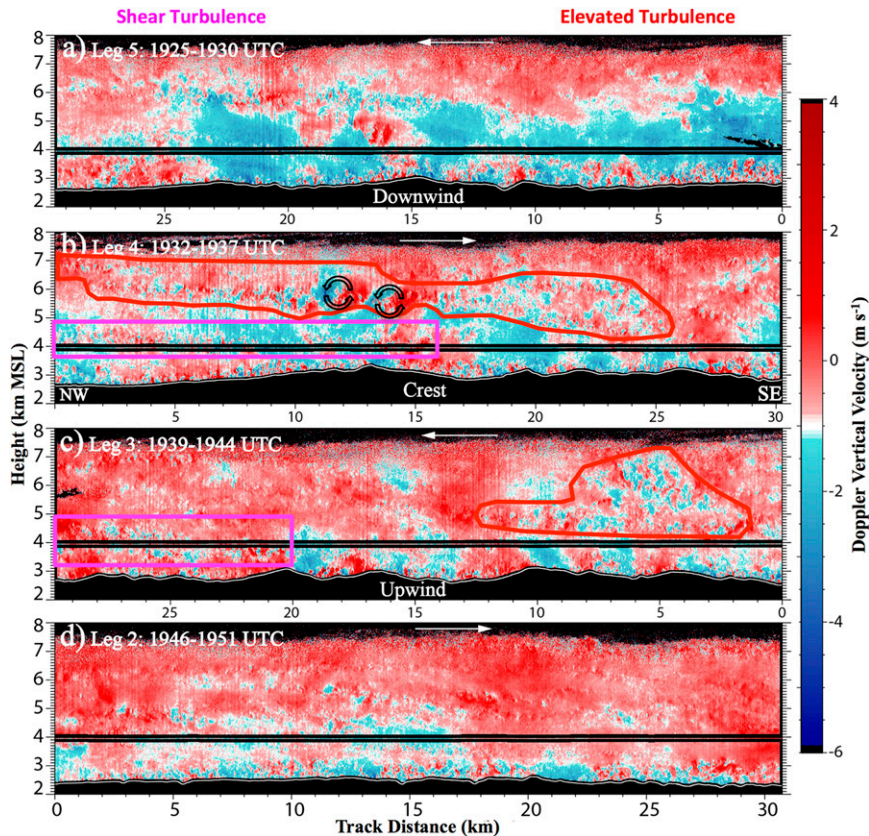


FIG. 13. Doppler vertical velocity measured by the WCR are plotted for UWKA research flight 4 (RF04) (a) leg 5, (b) leg 4, (c) leg 3, and (d) leg 2 of ladder 4 flown during 1925–1951 UTC 16 Jan 2012 (IOP2). The UWKA flight track is located within the radar blind zone (black) near 4 km MSL, and the underlying terrain is visible as the white line below the flight track. The 25-Hz vertical velocity measurements from in situ instruments aboard the UWKA are plotted within the WCR blind zone (near 4 km MSL). The flight tracks are all oriented northwest (NW) on the left and southeast (SE) on the right. The direction that the UWKA traveled across each leg is indicated by the white arrows. Note that track distances are slightly different for each flight leg. See Fig. 1a for flight leg locations. Notice that the Doppler vertical velocity color scale is centered at -1 m s^{-1} , which better depicts air motion as snow generally falls at $\sim 1 \text{ m s}^{-1}$. In situ vertical velocity (25-Hz data) plotted within the radar blind zone uses the same color scale but is centered at 0 m s^{-1} . The regions of shear turbulence (pink boxes) and elevated turbulence (red boundaries) are identified and discussed in the text. See text for further details.

indicates that little-to-weak turbulence was present, at least over Battle Pass (Fig. 10c).

UWKA flight legs 3 and 4 (1932–1944 UTC) also observed an elevated turbulent layer (red boundaries in Figs. 13b,c), which was also observed by the Battle Pass MRR as an increase in spectrum width near echo top (labeled in Fig. 10c). This elevated turbulence mainly contains subkilometer updrafts and downdrafts, but two larger ($\sim 1 \text{ km}$ wide) coherent overturning cells are observed in flight leg 4 between 5 and 6.5 km MSL with updrafts/downdrafts reaching $\pm 3 \text{ m s}^{-1}$ (see black arrows in Fig. 13b). It is unclear what induced these overturning cells, but the arrival of the cross-barrier jet during this time likely played a role, either through

releasing moist instability or creating shear instability above the jet.

The question is whether these turbulent layers affect the microphysical growth of snow particles. HM05 and MH15 suggest that localized enhancements of LWC are generated within the updrafts of observed turbulent overturning cells, which allow more rapid particle growth and fallout through aggregation and subsequent riming. During all flight legs shown in Fig. 13 (legs 2–5), in situ instruments aboard the UWKA observed no liquid water (not shown). Similarly, the microwave radiometer at Battle Pass observed ILW values $< 0.05 \text{ mm}$ (Fig. 4e) with LWC values $< 0.01 \text{ g m}^{-3}$ above 3.5 km MSL (Figs. 10b,c). However, during flight leg 1 between

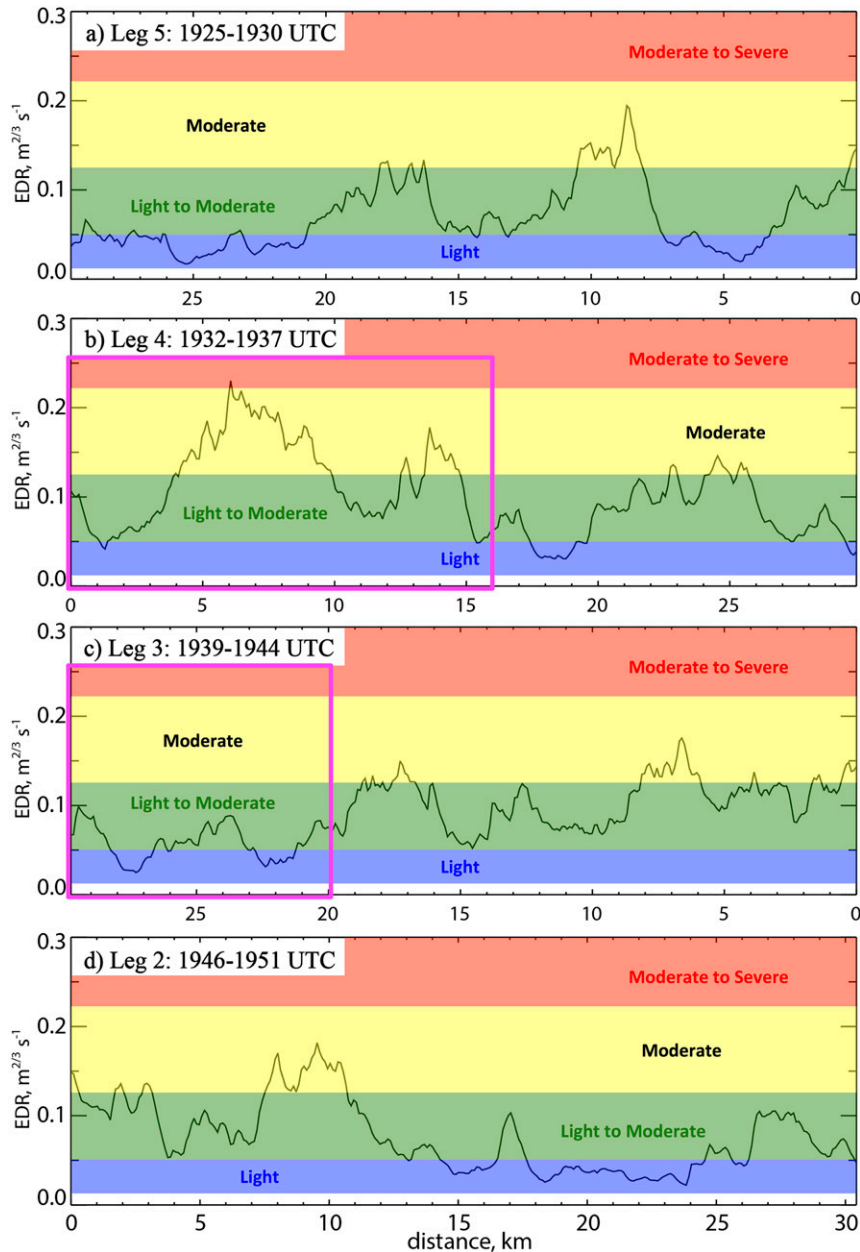


FIG. 14. EDR measured by the MacCready turbulence meter (MacCready 1964) aboard the UWKA is plotted for RF04 (a) leg 5, (b) leg 4, (c) leg 3, and (d) leg 2 of ladder 4 flown during 1925–1951 UTC 16 Jan 2012 (IOP2). Based on previous classifications (Strauss et al. 2015), EDR thresholds of 0.014, 0.050, 0.125, 0.220, 0.350, and $0.500 \text{ m}^{2/3} \text{ s}^{-1}$ designate smooth-to-light, light, light-to-moderate, moderate, moderate-to-severe, and severe turbulence categories, respectively. Regions where the UWKA flew through the layer of shear turbulence, indicated by the WCR Doppler velocity observations (Fig. 13), are outlined with a pink box, similar to Figs. 13 and 16. See text for more details.

1916 and 1921 UTC (Fig. 15), the CDP aboard the UWKA observed peaks in LWC up to 0.25 g m^{-3} at 4-, 7-, and 8.6-km flight distances (Fig. 15e). These LWC spikes are collocated with increased turbulence ($\text{EDR} > 0.15 \text{ m}^{2/3} \text{ s}^{-1}$; Fig. 15c), increased water vapor

mixing ratios (maximum is $\sim 1.57 \text{ g kg}^{-1}$; Fig. 15c), strong updrafts ($0.8\text{--}2.7 \text{ m s}^{-1}$; Figs. 15b,d), regions of lower reflectivity ($Z < 10 \text{ dBZ}$; Fig. 15a), and lower ice concentrations ($\sim 10 \text{ L}^{-1}$; Fig. 15e). These strong updrafts create increased cooling and condensation, thus

favoring the generation of supercooled liquid water. However, notice that no LWC was observed in an area of higher reflectivity ($Z > 10$ dBZ) and ice concentration ($40\text{--}50\text{ L}^{-1}$) where a similar strong updraft (1.6 m s^{-1}), increased turbulence (maximum EDR = $\sim 0.17\text{ m}^{2/3}\text{ s}^{-1}$), and increased mixing ratio (1.5 g kg^{-1}) were observed near a 23.5-km flight distance (red box; Fig. 15). One possible mechanism to explain this could be that larger and more numerous snow particles, generated at higher levels in the deep cloud and indicated by the higher Z and in situ ice concentration, fall through this layer of turbulent updrafts and grow through deposition. The cumulative consumption of water vapor from these larger and more numerous ice particles seems to prevent supercooled liquid water generation. The dominance of depositional growth agrees with the snow particles observed at the surface and the reflectivity profiles analyzed in section 4. Figure 16 reveals that reflectivity was high ($Z > 10$ dBZ) near the UWKA flight path during all flight legs shown in Fig. 13, especially within the turbulent shear layer between 3.6 and 4.7 km MSL (pink boxes in Figs. 13b,c and 16b,c), which explains why no in situ LWC was observed.

Although no in situ LWC observations are available within the elevated turbulence region, the elevated turbulence seems to occur in lower reflectivity regions ($Z < 10$ dBZ) with rapid reflectivity increases (fall streaks) extending below (Figs. 10a and 16b,c). Increased reflectivities were also observed by the WCR to extend from the center of the two overturning cells (Fig. 16b), indicating a net particle growth rather than offsetting growth and sublimation within the updraft and downdraft, respectively. These observations indicate that the elevated turbulence drove the majority of snow growth within this deep cloud system at the time of the UWKA flights. However, the observed large dendritic aggregates at Battle Pass during this time (section 4) indicate that the turbulent shear layer between 3.6 and 4.7 km MSL may have enhanced the aggregation of the snow particles falling from the elevated turbulence region. This agrees with the nearly uniform region of high reflectivity ($Z > 10$ dBZ) observed within the shear turbulence region (Figs. 16b,c) as aggregation would increase particle sizes and thus backscattered power.

Consistent increases in Z were observed by the MRR within and below the jet-induced turbulent shear layer during its peak strength between 2010 and 2120 UTC (Fig. 10). Vertical turrets of increased reflectivity above the main turbulent shear layer (3.6–4.5 km MSL) observed by the MRR at 2033, 2040, 2050, and 2056 UTC also seem to be collocated with weaker yet

enhanced turbulence up to 6 km MSL (Figs. 10a,c). Also note the decrease in Z observed by the MRR between 2040 and 2050 UTC (Fig. 10a). This temporary feature is collocated with a weakening of the plunging flow (Fig. 10b) and reduced shear turbulence (Fig. 10c), indicative of a weaker cross-barrier jet. Increased turbulence was also observed by the MRR below 4 km MSL, near the -15°C dendritic growth zone, before 1930 UTC and after 2125 UTC (Fig. 10c). This coincides with rapid reflectivity increases observed by the MRR (Fig. 10a) and DOW radar (Fig. 7a) below 4 km MSL and the presence of aggregates at the Battle Pass surface (Fig. 8).

Collectively, these observations suggest that the midlevel cross-barrier jet and its respective turbulent shear zone below the jet maximum are closely tied to turbulent overturning motion and rapid snow growth. These rapid snow growth regions frequently occur in pockets with distinct fall streaks extending below regions of increased turbulence. Snow growth due to the shear-induced turbulence occurred through deposition and aggregation due to the abundance of ice crystals from the deep, cold cloud system.

7. Discussion

The orographic precipitation system analyzed in this paper is similar to previously studied systems over the Park Range of Colorado. The postfrontal period analyzed in this analysis resembles the deep stratiform precipitation system depicted by the conceptual model shown in Fig. 13b of Rauber and Grant (1986). Similar to Rauber and Grant (1986), the deep clouds observed in this analysis contained very little liquid water. They suggest the reduction in liquid water is due to the increased ice crystal flux (concentration) from deeper and colder cloud tops, which increases the bulk diffusional growth rate and limits supercooled liquid water production. Observations from our analysis agree with this theory. Surface snow particles observed at Battle Pass are similar to snowfall observed by Rauber (1987), which mainly consisted of irregular and platelike crystals, dendrites, and aggregates, thus emphasizing the dominance of deposition and aggregation within these cold continental environments.

Previous observations have also indicated the importance of decoupled flow, namely low-level barrier jets and midlevel cross-barrier jets, for precipitation enhancement (e.g., Marwitz 1983; Overland and Bond 1995; Yu and Smull 2000; Yu and Bond 2002; Neiman et al. 2002, 2004; Loescher et al. 2006; Olson et al. 2007; Olson and Colle 2009). In the case analyzed here, the flow was decoupled but the northwesterly surface flow

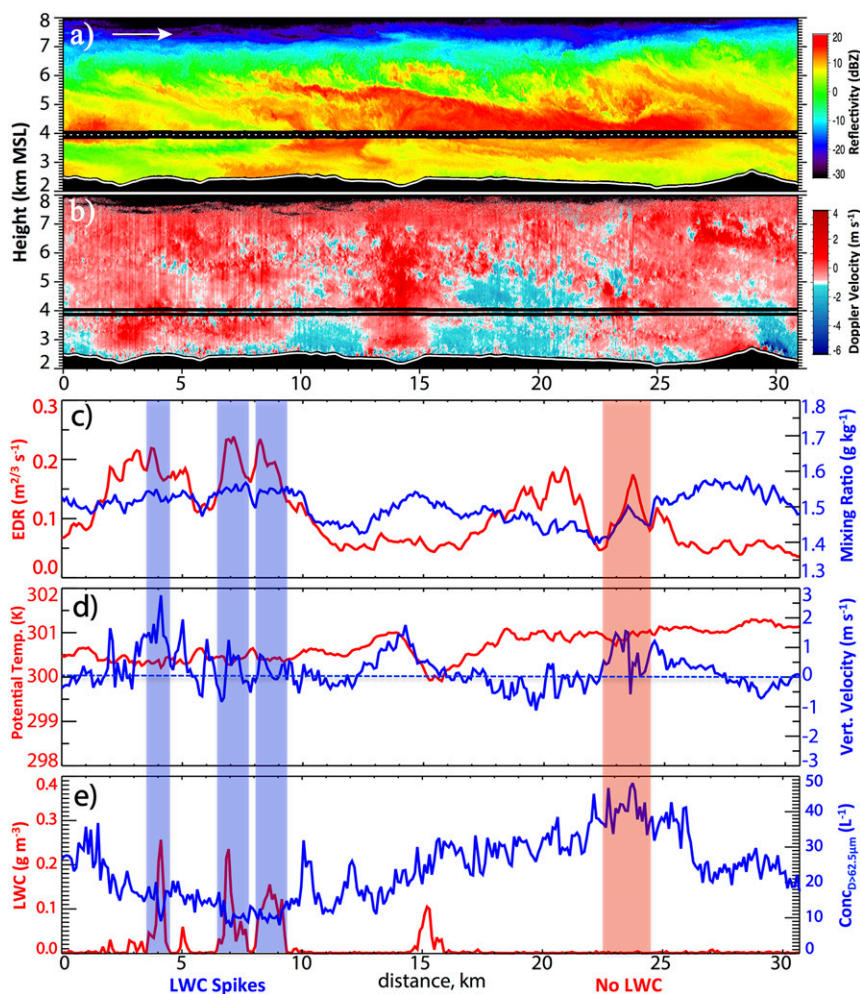


FIG. 15. WCR-observed (a) Z and (b) Doppler vertical velocity during 1916–1921 UTC 16 Jan 2012 for flight leg 1 of UWKA research flight 4, ladder 3. In situ measurements of (c) water vapor mixing ratio (g kg^{-1}) and EDR, (d) potential temperature (K) and vertical wind velocity (m s^{-1}), and (e) LWC (g m^{-3}) and ice concentration per liter (particle diameters from $62.5 \mu\text{m}$ to 2.5mm) are also shown. See Fig. 1a for ladder leg location. A blue dashed line in (d) marks the 0 m s^{-1} vertical wind velocity. Regions where vertical wind velocity is above this line identify updrafts, whereas downdrafts are located where vertical wind velocity lies below this line. See text for details.

in this case was part of the postfrontal air mass and not a result of deflected airflow. Medina and Houze (2003), HM05, and Rotunno and Houze (2007) discovered small-scale precipitation enhancements in overturning cells as a result of shear dynamic instability. Our observations agree with HM05 and MH15 in that increased turbulence favors increased snow growth, and that the presence of a cross-barrier jet favors increased turbulence through vertical wind shear. However, in the colder continental environment of Wyoming, enhanced depositional growth rather than riming was found to result from this shear-induced turbulence. Aggregation was observed at the surface when

1) enhanced growth aloft allowed larger snow particles to fall through the turbulent shear layer and 2) turbulence was located near the -15°C dendritic growth zone. The location of the midlevel cross-barrier jet and turbulent shear layer are similar to HM05 in that they formed at the top of a cold, decoupled surface layer. However, the decoupled surface layer in this analysis was associated with an Arctic air mass that extended above mountaintop rather than the blocked flows observed below mountaintop by HM05. In fact, the 2015 UTC sounding indicates some moist instability within the upwind decoupled surface layer (Fig. 3) and WCR along-barrier transects (Figs. 13, 15b) show air flowing

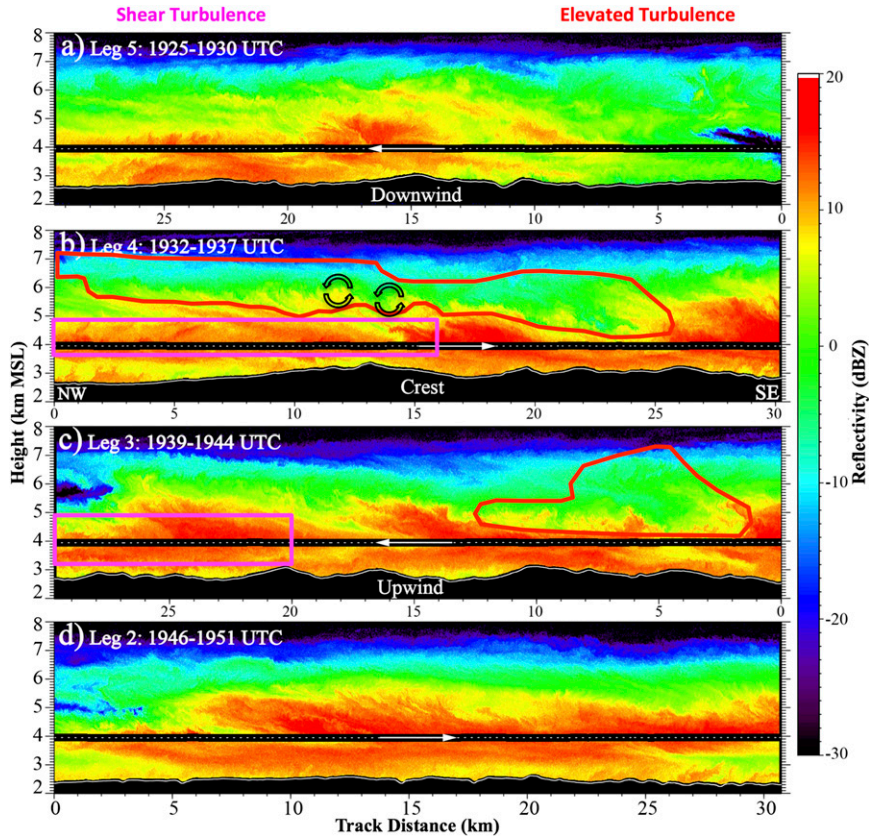


FIG. 16. As in Fig. 13, but for Z observed by the WCR. The UWKA flight track is plotted as a dotted white line within the radar blind zone. See Fig. 13 and text for further details.

up and over individual peaks within this decoupled surface layer (updrafts on northwest-facing slopes, downdrafts on southeast-facing slopes). HM05 also suggest that turbulent motions within the shear layer may cause small localized pockets of supercooled liquid water. Small pockets of supercooled liquid water were observed by the WCR in our case, but they were only observed outside regions of increased reflectivity and ice crystal concentration.

8. Conclusions

The role of turbulent shear instability associated with a postfrontal cross-barrier jet with regard to precipitation formation and fallout has been investigated using a suite of high-resolution ground-based and airborne radars and in situ instruments. Observations were taken during IOP2 (16 January 2012) of the 2012 ASCII field project in a deep, postfrontal winter orographic precipitation system over the Sierra Madre Range of Wyoming. Surface snow gauge observations at mountaintop (Battle Pass) indicated that 4 mm of liquid-equivalent precipitation fell during this postfrontal period

between 1910 and 2130 UTC with decreasing intensity ($1.3\text{--}2.9\text{ mm h}^{-1}$).

Dual-polarization radar-based analysis indicated that snow crystals primarily grew through water vapor deposition near cloud top and grew in size as particles fell to the ground, a primarily stratiform precipitation signal. Microwave radiometer and airborne in situ cloud physics probes measured little to no supercooled liquid water within the deep precipitating clouds. Enhanced reflectivity ($Z > 20\text{ dBZ}$) was advected from upwind of the target area between 1910 and 2105 UTC, which was associated with the arrival of a midlevel cross-barrier jet ($\sim 30\text{ m s}^{-1}$). Low-level ($< 4\text{ km MSL}$) reflectivity enhancements were observed within 15 km of the upwind side of the mountain between 2015 and 2130 UTC, likely due to rapid dendritic growth and aggregation. A post-frontal airmass inversion at 3.5 km MSL separated postfrontal northwesterly, along-barrier, slightly moist unstable flow from a southwesterly cross-barrier jet in stable air above. While wind shear characteristics were similar to previously observed blocked low-level flow, the northwesterly flow observed in the boundary layer in our analyzed case is part of the low-level postfrontal

Arctic air mass and not a result of deflected airflow. In fact, the Arctic air mass extended above mountaintop, yet orographic ascent upwind and plunging flow downwind was observed in the cross-barrier flow above.

Shear-induced turbulence and overturning cells were observed between the top of this Arctic air mass and the cross-barrier jet maximum wind speed ($\sim 30 \text{ ms}^{-1}$). An elevated layer of turbulent overturning cells was also observed by the WCR earlier in the analysis period and collocated with the arrival of the midlevel cross-barrier jet. These turbulent regions created pockets of rapid snow growth through enhanced depositional and aggregational processes. No liquid water was observed in the vicinity of the overturning cells, as suggested by HM05 and MH15. The lack of liquid water is likely due to the increased concentration of ice particles falling from the deeper cloud above, which consumes water vapor too fast to allow liquid drops to grow. This hypothesis is supported by previous research (Raubert and Grant 1986) and WCR and in situ UWKA data, which show that turbulent updrafts favor cooling and liquid water generation, but only outside regions of increased reflectivity and ice crystal concentration.

Previous studies investigating the role of shear dynamic instability on precipitation formation have focused on events with large moisture fluxes and the presence of supercooled liquid water along more coastal mountain ranges (HM05; MH15). This study highlighted the effects of shear dynamic instability on snow growth for an inner-mountain range with lower moisture flux and the absence of supercooled liquid water. The analysis presented in this paper also focuses on a smaller mountain range, whereas previous research has focused on larger mountain barriers.

The results of this paper suggest that 1) shear-induced turbulent overturning cells do exist over cold continental mountain ranges such as the Sierra Madre Range, 2) the presence of cross-barrier jets favor these turbulent shear zones, 3) this turbulence is a key mechanism in enhancing snow growth, and 4) snow growth enhanced by turbulence primarily occurs through deposition and aggregation in these cold ($< -15^\circ\text{C}$) postfrontal continental environments.

Acknowledgments. We thank the Center for Severe Weather Research staff for recording and processing the DOW radar data, Mike Dixon at NCAR for assisting with the Radx radar software, Evan Kalina and Yang Yang for taking snow crystal photographs at Battle Pass, Samuel Haimov, Yang Yang, and Xiaoqin Jing for providing the IDL analysis code for the WCR data and WCR radar specifications used in ASCII, and the

anonymous reviewers for their helpful suggestions to improve this paper. This work was partially supported by the AMS Graduate Fellowship Program and the Cooperative Institute for Research in Environmental Sciences (CIRES). The ASCII experiment was a collaborative field study between the University of Wyoming, University of Colorado Boulder, NCAR, and the University of Illinois at Urbana-Champaign and funded through NSF Grant AGS-1058426. Any opinions, findings, or recommendations expressed in this publication are those of the authors and do not necessarily reflect the views of the National Science Foundation.

REFERENCES

- Andrić, J., D. Zrnić, J. M. Straka, and V. Melnikov, 2010: The enhanced Z_{DR} signature in stratiform clouds above melting layer. *13th Conf. on Cloud Physics*, Portland, OR, Amer. Meteor. Soc., P2.89. [Available online at <https://ams.confex.com/ams/pdfpapers/171308.pdf>.]
- , M. R. Kumjian, D. S. Zrnić, J. M. Straka, and V. M. Melnikov, 2013: Polarimetric signatures above the melting layer in winter storms: An observational and modeling study. *J. Appl. Meteor. Climatol.*, **52**, 682–700, doi:10.1175/JAMC-D-12-028.1.
- Bailey, M. P., and J. Hallett, 2009: A comprehensive habit diagram for atmospheric ice crystals: Confirmation from the laboratory, AIRS II, and other field studies. *J. Atmos. Sci.*, **66**, 2888–2899, doi:10.1175/2009JAS2883.1.
- Battaglia, A., E. Rustemeier, A. Tokay, U. Blahak, and C. Simmer, 2010: PARSIVEL snow observations: A critical assessment. *J. Atmos. Oceanic Technol.*, **27**, 333–344, doi:10.1175/2009JTECHA1332.1.
- Bechini, R., L. Baldini, and V. Chandrasekar, 2013: Polarimetric radar observations in the ice region of precipitating clouds at C-band and X-band radar frequencies. *J. Appl. Meteor. Climatol.*, **52**, 1147–1169, doi:10.1175/JAMC-D-12-055.1.
- Brandes, E. A., K. Ikeda, G. Zhang, M. Schönhuber, and R. M. Rasmussen, 2007: A statistical and physical description of hydrometeor distributions in Colorado snowstorms using a video disdrometer. *J. Appl. Meteor. Climatol.*, **46**, 634–650, doi:10.1175/JAM2489.1.
- , —, G. Thompson, and M. Schönhuber, 2008: Aggregate terminal velocity/temperature relations. *J. Appl. Meteor. Climatol.*, **47**, 2729–2736, doi:10.1175/2008JAMC1869.1.
- Friedrich, K., E. A. Kalina, F. J. Masters, and C. R. Lopez, 2013: Drop-size distributions in thunderstorms measured by optical disdrometers during VORTEX2. *Mon. Wea. Rev.*, **141**, 1182–1203, doi:10.1175/MWR-D-12-00116.1.
- Garvert, M. F., B. Smull, and C. Mass, 2007: Multiscale mountain waves influencing a major orographic precipitation event. *J. Atmos. Sci.*, **64**, 711–737, doi:10.1175/JAS3876.1.
- Geerts, B., R. Damiani, and S. Haimov, 2006: Finescale vertical structure of a cold front as revealed by an airborne Doppler radar. *Mon. Wea. Rev.*, **134**, 251–271, doi:10.1175/MWR3056.1.
- , Q. Miao, and Y. Yang, 2011: Boundary layer turbulence and orographic precipitation growth in cold clouds: Evidence from profiling airborne radar data. *J. Atmos. Sci.*, **68**, 2344–2365, doi:10.1175/JAS-D-10-05009.1.

- , and Coauthors, 2013: The AgI Seeding Cloud Impact Investigation (ASCI) campaign 2012: Overview and preliminary results. *J. Wea. Modif.*, **45**, 24–43.
- , Y. Yang, R. Rasmussen, S. Haimov, and B. Pokharel, 2015: Snow growth and transport patterns in orographic storms as estimated from airborne vertical-plane dual-Doppler radar data. *Mon. Wea. Rev.*, **143**, 644–665, doi:10.1175/MWR-D-14-00199.1.
- Gourley, J. J., P. Tabary, and J. Parent du Chatelet, 2007: A fuzzy logic algorithm for the separation of precipitating from non-precipitating echoes using polarimetric radar observations. *J. Atmos. Oceanic Technol.*, **24**, 1439–1451, doi:10.1175/JTECH2035.1.
- Hindman, E. E., 1986: Characteristics of supercooled liquid water in clouds at mountaintop sites in the Colorado Rockies. *J. Climate Appl. Meteor.*, **25**, 1271–1279, doi:10.1175/1520-0450(1986)025<1271:COSLWI>2.0.CO;2.
- Hogan, R. J., P. R. Field, A. J. Illingworth, R. J. Cotton, and T. W. Choullarton, 2002: Properties of embedded convection in warm-frontal mixed-phase cloud from aircraft and polarimetric radar. *Quart. J. Roy. Meteor. Soc.*, **128**, 451–476, doi:10.1256/003590002321042054.
- Houze, R. A., and S. Medina, 2005: Turbulence as a mechanism for orographic precipitation enhancement. *J. Atmos. Sci.*, **62**, 3599–3623, doi:10.1175/JAS3555.1.
- Hovmöller, E., 1949: The trough-and-ridge diagram. *Tellus*, **1**, 62–66, doi:10.1111/j.2153-3490.1949.tb01260.x.
- Jing, X., and B. Geerts, 2015: Dual-polarization radar data analysis of the impact of ground-based glaciogenic seeding on winter orographic clouds. Part II: Convective clouds. *J. Appl. Meteor. Climatol.*, **54**, 2099–2117, doi:10.1175/JAMC-D-15-0056.1.
- , —, K. Friedrich, and B. Pokharel, 2015: Dual-polarization radar data analysis of the impact of ground-based glaciogenic seeding on winter orographic clouds. Part I: Mostly stratiform clouds. *J. Appl. Meteor. Climatol.*, **54**, 1944–1969, doi:10.1175/JAMC-D-14-0257.1.
- Kennedy, P. C., and S. A. Rutledge, 2011: S-band dual-polarization radar observations of winter storms. *J. Appl. Meteor. Climatol.*, **50**, 844–858, doi:10.1175/2010JAMC2558.1.
- Kirshbaum, D. J., G. H. Bryan, R. Rotunno, and D. R. Durran, 2007: The triggering of orographic rainbands by small-scale topography. *J. Atmos. Sci.*, **64**, 1530–1549, doi:10.1175/JAS3924.1.
- Kumjian, M. R., S. A. Rutledge, R. M. Rasmussen, P. C. Kennedy, and M. Dixon, 2014: High-resolution polarimetric radar observations of snow-generating cells. *J. Appl. Meteor. Climatol.*, **53**, 1636–1658, doi:10.1175/JAMC-D-13-0312.1.
- Lamb, D., and J. Verlinde, 2011: *Physics and Chemistry of Clouds*. Cambridge University Press, 584 pp.
- Locatelli, J. D., and P. V. Hobbs, 1974: Fall speeds and masses of solid precipitation particles. *J. Geophys. Res.*, **79**, 2185–2197, doi:10.1029/JC079i015p02185.
- Loescher, K. A., G. S. Young, B. A. Colle, and N. S. Winstead, 2006: Climatology of barrier jets along the Alaskan coast. Part I: Spatial and temporal distributions. *Mon. Wea. Rev.*, **134**, 437–453, doi:10.1175/MWR3037.1.
- Löffler-Mang, M., M. Kunz, and W. Schmid, 1999: On the performance of a low-cost K-band Doppler radar for quantitative rain measurements. *J. Atmos. Oceanic Technol.*, **16**, 379–387, doi:10.1175/1520-0426(1999)016<0379:OTPOAL>2.0.CO;2.
- Maahn, M., and P. Kollias, 2012: Improved Micro Rain Radar snow measurements using Doppler spectra post-processing. *Atmos. Meas. Tech.*, **5**, 2661–2673, doi:10.5194/amt-5-2661-2012.
- MacCready, P. B., 1964: Standardization of gustiness values from aircraft. *J. Appl. Meteor.*, **3**, 439–449, doi:10.1175/1520-0450(1964)003<0439:SOGVFA>2.0.CO;2.
- Marwitz, J. D., 1983: The kinematics of orographic airflow during Sierra storms. *J. Atmos. Sci.*, **40**, 1218–1227, doi:10.1175/1520-0469(1983)040<1218:TKOOAD>2.0.CO;2.
- Medina, S., and R. A. Houze, 2003: Air motions and precipitation growth in Alpine storms. *Quart. J. Roy. Meteor. Soc.*, **129**, 345–371, doi:10.1256/qj.02.13.
- , and —, 2015: Small-scale precipitation elements in mid-latitude cyclones crossing the California Sierra Nevada. *Mon. Wea. Rev.*, **143**, 2842–2870, doi:10.1175/MWR-D-14-00124.1.
- , B. F. Smull, R. A. Houze, and M. Steiner, 2005: Cross-barrier flow during orographic precipitation events: Results from MAP and IMPROVE. *J. Atmos. Sci.*, **62**, 3580–3598, doi:10.1175/JAS3554.1.
- Moisseev, D., E. Saltikoff, and M. Leskinen, 2009: Dual-polarization weather radar observations of snow growth processes. *34th Conf. on Radar Meteor.*, Williamsburg, VA, Amer. Meteor. Soc., 13B.2. [Available online at <https://ams.confex.com/ams/pdfpapers/156123.pdf>.]
- Neiman, P. J., F. M. Ralph, A. B. White, D. E. Kingsmill, and P. O. G. Persson, 2002: The statistical relationship between upslope flow and rainfall in California's Coastal Mountains: Observations during CALJET. *Mon. Wea. Rev.*, **130**, 1468–1492, doi:10.1175/1520-0493(2002)130<1468:TSRBUF>2.0.CO;2.
- , —, P. O. G. Persson, A. B. White, D. P. Jorgensen, and D. E. Kingsmill, 2004: Modification of fronts and precipitation by coastal blocking during an intense landfalling winter storm in Southern California: Observations during CALJET. *Mon. Wea. Rev.*, **132**, 242–273, doi:10.1175/1520-0493(2004)132<0242:MOFAPB>2.0.CO;2.
- Olson, J. B., and B. A. Colle, 2009: Three-dimensional idealized simulations of barrier jets along the southeast coast of Alaska. *Mon. Wea. Rev.*, **137**, 391–413, doi:10.1175/2008MWR2480.1.
- , —, N. A. Bond, and N. Winstead, 2007: A comparison of two coastal barrier jet events along the southeast Alaskan coast during the SARJET field experiment. *Mon. Wea. Rev.*, **135**, 3642–3663, doi:10.1175/MWR3448.E1.
- Overland, J. E., and N. A. Bond, 1995: Observations and scale analysis of coastal wind jets. *Mon. Wea. Rev.*, **123**, 2934–2941, doi:10.1175/1520-0493(1995)123<2934:OASAO>2.0.CO;2.
- Peters, G., B. Fischer, and T. Andersson, 2002: Rain observations with a vertically looking Micro Rain Radar (MRR). *Boreal Environ. Res.*, **7**, 353–362.
- , —, H. Münster, M. Clemens, and A. Wagner, 2005: Profiles of raindrop size distributions as retrieved by microrain radars. *J. Appl. Meteor.*, **44**, 1930–1949, doi:10.1175/JAM2316.1.
- Plummer, D. M., G. M. McFarquhar, R. M. Rauber, B. F. Jewett, and D. C. Leon, 2014: Structure and statistical analysis of the microphysical properties of generating cells in the comma head region of continental winter cyclones. *J. Atmos. Sci.*, **71**, 4181–4203, doi:10.1175/JAS-D-14-0100.1.
- Pokharel, B., B. Geerts, and X. Jing, 2014a: The impact of ground-based glaciogenic seeding on orographic clouds and precipitation: A multisensor case study. *J. Appl. Meteor. Climatol.*, **53**, 890–909, doi:10.1175/JAMC-D-13-0290.1.
- , —, —, K. Friedrich, J. Aikins, D. Breed, R. Rasmussen, and A. Huggins, 2014b: The impact of ground-based glaciogenic seeding on clouds and precipitation over mountains: A multi-sensor case study of shallow precipitating orographic cumuli. *Atmos. Res.*, **147–148**, 162–182, doi:10.1016/j.atmosres.2014.05.014.

- , —, and —, 2015: The impact of ground-based glaciogenic seeding on clouds and precipitation over mountains: A case study of a shallow orographic cloud with large supercooled droplets. *J. Geophys. Res. Atmos.*, **120**, 6056–6079, doi:[10.1002/2014JD022693](https://doi.org/10.1002/2014JD022693).
- Rauber, R. M., 1987: Characteristics of cloud ice and precipitation during wintertime storms over the mountains of northern Colorado. *J. Climate Appl. Meteor.*, **26**, 488–524, doi:[10.1175/1520-0450\(1987\)026<0488:COCIAP>2.0.CO;2](https://doi.org/10.1175/1520-0450(1987)026<0488:COCIAP>2.0.CO;2).
- , 1992: Microphysical structure and evolution of a central Sierra Nevada orographic cloud system. *J. Appl. Meteor.*, **31**, 3–24, doi:[10.1175/1520-0450\(1992\)031<0003:MSAEOA>2.0.CO;2](https://doi.org/10.1175/1520-0450(1992)031<0003:MSAEOA>2.0.CO;2).
- , and L. O. Grant, 1986: The characteristics and distribution of cloud water over the mountains of northern Colorado during wintertime storms. Part II: Spatial distribution and microphysical characteristics. *J. Climate Appl. Meteor.*, **25**, 489–504, doi:[10.1175/1520-0450\(1986\)025<0489:TCADOC>2.0.CO;2](https://doi.org/10.1175/1520-0450(1986)025<0489:TCADOC>2.0.CO;2).
- Rollenbeck, R., J. Bendix, P. Fabian, J. Boy, W. Wilcke, H. Dalitz, M. Oesker, and P. Emck, 2007: Comparison of different techniques for the measurement of precipitation in tropical montane rain forest regions. *J. Atmos. Oceanic Technol.*, **24**, 156–168, doi:[10.1175/JTECH1970.1](https://doi.org/10.1175/JTECH1970.1).
- Rosenkranz, P. W., 1998: Water vapor microwave continuum absorption: A comparison of measurements and models. *Radio Sci.*, **33**, 919–928, doi:[10.1029/98RS01182](https://doi.org/10.1029/98RS01182).
- Rosenow, A. A., D. M. Plummer, R. M. Rauber, G. M. McFarquhar, B. F. Jewett, and D. Leon, 2014: Vertical velocity and physical structure of generating cells and convection in the comma head region of continental winter cyclones. *J. Atmos. Sci.*, **71**, 1538–1558, doi:[10.1175/JAS-D-13-0249.1](https://doi.org/10.1175/JAS-D-13-0249.1).
- Rotunno, R., and R. A. Houze, 2007: Lessons on orographic precipitation from the Mesoscale Alpine Programme. *Quart. J. Roy. Meteor. Soc.*, **133**, 811–830, doi:[10.1002/qj.67](https://doi.org/10.1002/qj.67).
- Ryzhkov, A. V., and D. S. Zrnić, 1998: Discrimination between rain and snow with a polarimetric radar. *J. Appl. Meteor.*, **37**, 1228–1240, doi:[10.1175/1520-0450\(1998\)037<1228:DBRASW>2.0.CO;2](https://doi.org/10.1175/1520-0450(1998)037<1228:DBRASW>2.0.CO;2).
- Saleeby, S. M., W. R. Cotton, and J. D. Fuller, 2011: The cumulative impact of cloud droplet nucleating aerosols on orographic snowfall in Colorado. *J. Appl. Meteor. Climatol.*, **50**, 604–625, doi:[10.1175/2010JAMC2594.1](https://doi.org/10.1175/2010JAMC2594.1).
- , —, D. Lowenthal, and J. Messina, 2013: Aerosol impacts on the microphysical growth processes of orographic snowfall. *J. Appl. Meteor. Climatol.*, **52**, 834–852, doi:[10.1175/JAMC-D-12-0193.1](https://doi.org/10.1175/JAMC-D-12-0193.1).
- Schneebeil, M., N. Dawes, M. Lehning, and A. Berne, 2013: High-resolution vertical profiles of X-band polarimetric radar observables during snowfall in the Swiss Alps. *J. Appl. Meteor. Climatol.*, **52**, 378–394, doi:[10.1175/JAMC-D-12-015.1](https://doi.org/10.1175/JAMC-D-12-015.1).
- Smith, R. B., and Coauthors, 2012: Orographic precipitation in the tropics: The Dominica Experiment. *Bull. Amer. Meteor. Soc.*, **93**, 1567–1579, doi:[10.1175/BAMS-D-11-00194.1](https://doi.org/10.1175/BAMS-D-11-00194.1).
- Solheim, F., J. Godwin, and R. Ware, 1998a: Passive ground-based remote sensing of atmospheric temperature, water vapor, and cloud liquid water profiles by a frequency synthesized microwave radiometer. *Meteor. Z.*, **7**, 370–376.
- , —, E. Westwater, Y. Han, S. Keilm, K. Marsh, and R. Ware, 1998b: Radiometric profiling of temperature, water vapor and cloud liquid water using various inversion methods. *Radio Sci.*, **33**, 393–404, doi:[10.1029/97RS03656](https://doi.org/10.1029/97RS03656).
- Strauss, L., S. Serafin, S. Haimov, and V. Grubišić, 2015: Turbulence in breaking mountain waves and atmospheric rotors estimated from airborne in situ and Doppler radar measurements. *Quart. J. Roy. Meteor. Soc.*, **141**, 3207–3225, doi:[10.1002/qj.2604](https://doi.org/10.1002/qj.2604).
- Tokay, A., P. Hartmann, A. Battaglia, K. S. Gage, W. L. Clark, and C. R. Williams, 2009: A field study of reflectivity and Z–R relations using vertically pointing radars and disdrometers. *J. Atmos. Oceanic Technol.*, **26**, 1120–1134, doi:[10.1175/2008JTECHA1163.1](https://doi.org/10.1175/2008JTECHA1163.1).
- Trivej, P., and B. Stevens, 2010: The echo size distribution of precipitating shallow cumuli. *J. Atmos. Sci.*, **67**, 788–804, doi:[10.1175/2009JAS3178.1](https://doi.org/10.1175/2009JAS3178.1).
- Wang, Z., and Coauthors, 2012: Single aircraft integration of remote sensing and in situ sampling for the study of cloud microphysics and dynamics. *Bull. Amer. Meteor. Soc.*, **93**, 653–668, doi:[10.1175/BAMS-D-11-00044.1](https://doi.org/10.1175/BAMS-D-11-00044.1).
- Wurman, J., 2001: The DOW mobile multiple-Doppler network. Preprints, *30th Int. Conf. on Radar Meteorology*, Munich, Germany, Amer. Meteor. Soc., 95–97.
- Yu, C.-K., and B. F. Smull, 2000: Airborne Doppler observations of a landfalling cold front upstream of steep coastal orography. *Mon. Wea. Rev.*, **128**, 1577–1603, doi:[10.1175/1520-0493\(2000\)128<1577:ADOOAL>2.0.CO;2](https://doi.org/10.1175/1520-0493(2000)128<1577:ADOOAL>2.0.CO;2).
- , and N. A. Bond, 2002: Airborne Doppler observations of a cold front in the vicinity of Vancouver Island. *Mon. Wea. Rev.*, **130**, 2692–2708, doi:[10.1175/1520-0493\(2002\)130<2692:ADOOAC>2.0.CO;2](https://doi.org/10.1175/1520-0493(2002)130<2692:ADOOAC>2.0.CO;2).